Low-level wind variability at Jaisalmer and its representation in ERA5 Reanalysis

Bela Lodh[1], Vishal Dixit[1*], G. S. Bhat[2], Pramit Kumar Deb Burman[3]

[1] Centre for Climate Studies, Indian Institute of Technology, Bombay, India

[2] Centre for Atmospheric and Oceanic Sciences, Indian Institute of Science, Bangalore, India

[3] Centre for Climate Change Research, Indian Institute of Tropical Meteorology, Pune, India

Emails - belaalodh@gmail.com; bhat@iisc.ac.in; pramit.cat@tropmet.res.in

*Email for correspondence – vdixit@iitb.ac.in

Peer-review status: This is a non-peer-reviewed preprint submitted to EarthArXiv.

Low-level wind variability at Jaisalmer and its representation in ERA5 Reanalysis

Bela Lodh[1], Vishal Dixit[1], G. S. Bhat[2], and Pramit Kumar Deb Burman[3]

[1]Centre for Climate Studies, Indian Institute of Technology Bombay, Mumbai, India
[2]Centre for Atmospheric and Oceanic Sciences, Indian Institute of Science, Bengaluru, India
[3]Indian Institute of Tropical Meteorology, Pune, India

Abstract

Jaisalmer has grown to be one of the important wind energy hubs in India following the development of the Jaisalmer Wind Park. In this study we assess the variability of wind speed at various scales, and the occurrence of wind ramps (defined as the change in wind speed over a certain period) at Jaisalmer using high-quality in-situ measurements. A distinct diurnal pattern in wind ramps is seen in winter as the wind speeds show a small but sudden rise in the morning hours and a drop in the late afternoons. This pattern is absent in the summer months but re-emerges briefly during August which is the peak of the local summer monsoon season. Version 5 of the global climate reanalysis by the European Centre for Medium-Range Weather Forecasts (ERA5) underestimates the magnitude of wind ramps and misrepresents their diurnal timing, with the peak occurrence shifted. Land-atmosphere interactions are critical in shaping wind dynamics within the planetary boundary layer, particularly through their influence on the turbulent processes, that are pronounced in the surface layer where wind turbines are placed. According to widely adopted bulk parameterizations, the sensible heat flux (SHF) at the surface is parameterized in terms of wind speed (U) and temperature difference (DT) between the surface and the reference altitude. Numerous modifications pertaining to different scaling approaches have been proposed to this parameterization to improve the model accuracy under various conditions. In this study, we found that during night hours, the SHF downward to the land is strongly coupled with U by a linear relationship that is particularly pronounced in winter and absent during summer. Moreover, the periods of prominent nighttime correlation coincide precisely with the ramp-free hours. After sunrise, the boundary layer undergoes a transition from forced to mixed convective regime leading to a brief period of linear coupling between the SHF and U from 12 AM to 4 PM. Unlike the nighttime regime that is a feature of winters and spans a duration of nearly 12 hours, the daytime regime is observed during summer over a shorter temporal scale. We find that the stable wind regime during night is captured in ERA5 successfully, while the daytime regimes need a significant improvement in representation.

Keywords: Near-surface wind speed, wind ramps, surface sensible heat flux, bulk parameterizations, wind energy

1 Introduction

With the increasing energy requirements of the rapidly growing and technologically advancing global population (1), the whole world is recognising the importance of renewable sources of energy, particularly wind energy (2). Many countries around the world are expanding their capacity for wind power generation (3), (4) and recent developments in India's installed onshore wind power capacity have been appreciable (5), (6), (7), (8), (9). Among several Indian states, the installed capacity at Rajasthan has increased manifold in recent decades (10). The geographical positioning of a location and the topographical features in its vicinity heavily impact the climatology of winds, and the wind power potential, a popular measure of which is the wind power density (11). The western part of Rajasthan

is considered a viable location for wind farms due to its high wind power density (12), (13), (14). In addition, the predominant geomorphological feature being sandy dunes makes the land uncultivable, and the hard terrain makes it ideal for the installation of windmills (15). This rapid expansion of wind power infrastructure in Rajasthan was exemplified by the development of the Jaisalmer Wind Park (JWP). With an installed capacity of 1,064 MW, the JWP is India's second largest and globally the fourth largest offshore wind facility (16). Thus, an assessment of the spatiotemporal regimes of wind speed at Jaisalmer is crucial to enhance the accuracy of forecasts of energy generation and the effectiveness of grid integration. In this study, we characterise the wind speed and its mean diurnal variability, often referred to as wind ramps which play a crucial role in determining the operational efficiency of wind turbines and improving short-term energy generation forecasts.

A crucial yet less explored aspect of prevailing wind patterns at a location is the underlying surface-atmosphere interactions. Land-atmosphere interactions (mainly in the forms of heat and momentum exchange) shape wind dynamics within the planetary boundary layer, particularly through turbulence processes that are pronounced in the surface layer where wind turbines are situated. Heat fluxes at the surface impact the thermal stability within the column which in turn determines the turbulence and mixing within the boundary layer. A thermally stable boundary layer suppresses vertical transfer of momentum, leading to a pronounced environmental wind shear which is absent in well-mixed environments. A detailed understanding of land-atmosphere interactions and identifying distinct regimes allows the development of finely tuned regime-aware bulk parameterizations and improved model forecasts. Sensible heat flux at the surface is parameterized in terms of wind speed and the temperature difference between the surface and a near-surface layer of the atmosphere. The widely used bulk formula is given as

$$\mathrm{SHF} = \rho\, c_p\, C_H\, U\, \Delta T \tag{1}$$

where SHF is the dynamic form of the sensible heat flux at the surface (in units of $\mathrm{W\,m^{-2}}$), ρ is the air density ($\mathrm{kg\,m^{-3}}$), c_p is the specific heat capacity at constant pressure ($\mathrm{J\,kg^{-1}\,K^{-1}}$), C_H is the bulk heat transfer coefficient (dimensionless), U is the wind speed at the reference height ($\mathrm{m\,s^{-1}}$) and ΔT is the temperature difference between the surface and the reference height (K or °C).

The Monin–Obukhov Similarity Theory (MOST) prescribes a framework to relate the bulk heat transfer coefficient C_H to surface roughness and the state of stability of the atmospheric column. Thus, the parameterization becomes applicable across different stability regimes. Observational field campaigns continue to contribute to our understanding of different regimes, based on which numerous modifications pertaining to different scaling approaches have been proposed to this parameterization to improve model accuracy in varied conditions (MONTBLEX-90 (17),(18), (19), INCOMPASS (20), FLUXNET (21), INFLUX (22), MONEX (23), CASES-99 (24), SLTEST (25)). A widely known limitation of the MOST framework is that it is unsuccessful in parameterizing SHF as we transition from mixed to free-convection regime. According to Eq. 1, the modeled SHF decreases with wind speed and tends to take values lower than those at the free convection limit. (26), (27) proposed that we identify this transitional regime as a "weakly forced" or "near-free" convective regime where Townsend's scaling for the free convective limit may be applicable. According to this scaling, SHF is independent of wind speed and is instead given by

$$\mathrm{SHF} = \overline{w'\theta'}_s = C_s \left(\frac{g}{\theta_m}\,\frac{\kappa^2}{\nu}\right)^{1/3} (\Delta T)^{4/3} \tag{2}$$

where κ is the molecular thermal diffusivity, ν is the kinematic viscosity, θ_m is the (constant) potential temperature within the mixed layer, g is the acceleration due to gravity, $\overline{w'\theta'}_s$ represents the average eddy sensible heat flux, and C_s is an empirical constant. Analogous to the convective regime where SHF is parameterized solely in terms of ΔT, we examine its dependence on wind speed alone across different stability regimes, with a particular focus on the nocturnal stable boundary layer. To the best of our knowledge, not many studies have been conducted so far to understand wind regimes along with

land-atmosphere interactions at Jaisalmer in view of its rapid development as a wind energy hub. In this study, we analyse a high quality observational dataset to address this problem. Additionally, we also evaluate the widely used ERA5 reanalysis dataset in reproducing these regimes.

Reanalysis data sets are increasingly being used to understand meteorological variables and even in renewable energy forecasts (28), (29). Among the different reanalysis datasets, the European Centre for Medium-Range Weather Forecasts' ERA5 has been shown to be particularly useful in wind power forecasts (30), (31), (32), (33), (34), (35), (36), (37). Some studies have shown that regional reanalysis datasets with finer resolutions outperform ERA5 in terms of local accuracy (38), (39), (40), (41). For example, the COSMO-REA6 dataset (spatial resolution 6 km) better resolves local wind patterns in regions with complex orography and coastlines (42). However, in instances of unavailability of regional data, ERA5 is widely considered reliable (43), (44), (45). Due to the skill consistently demonstrated by ERA5 in wind power modeling, especially compared to prior reanalysis data sets, it is being used as training data for machine learning-based models (46). Recent work finds that ERA5 better captures the amplitude of daily wind variation at hub height than its predecessors, and this forms an essential attribute for a training dataset to emulate diurnal and stability-driven variability (47), particularly for a semi-arid site like Jaisalmer. Comparative assessments note that reanalyses capture multidecadal mean wind patterns with small biases, but local regime mismatches remain (48), (49), (50); ERA5's improved resolution and physics make it preferable as a feature source for ML while still necessitating local calibration (51).

In summary of our objectives, we analyze high-quality observational data from Jaisalmer to identify dominant wind regimes in terms of standard aspects including annual and diurnal variability and the occurrence of wind ramps. Along with this, we find different regimes in the coupling between low-level wind speed and the sensible heat flux at the surface. At each step, we evaluate how well ERA5 reanalysis reproduces these observed regimes in order to assess its suitability as a resource for wind energy applications in semi-arid regions such as Jaisalmer. Lastly, we show the spatial extent of the applicability of our results over the landmass of India.

2 Datasets and Methodology

2.1 Observational Datasets

Near-surface air temperature (T, °C), air pressure (P, hPa), wind speed (U, $\mathrm{m\,s^{-1}}$), surface sensible heat flux in its dynamic form (SHF, $\mathrm{W\,m^{-2}}$), and surface stress (τ, $\mathrm{N\,m^{-2}}$ or $\mathrm{kg\,m^{-1}\,s^{-2}}$) was obtained from an eddy covariance flux tower located at the Central Arid Zone Research Institute (CAZRI), Jaisalmer (26.99°N, 71.34°E), for 2017 at a temporal frequency of 15 minutes. This site, part of the Interaction of Convective Organization and Monsoon Precipitation, Atmosphere, Surface and Sea (INCOMPASS) field campaign, is characterized by natural vegetation, predominantly Sewan grass, and represents a semi-arid region in northwestern India. Measurements were made using an EC150 (Irgason) eddy covariance system mounted at approximately 8 m above the ground level. A detailed description of the site characteristics, instrumentation, and data processing protocols is provided in (52).

For the observed values of land surface temperature (LST), we used the publicly available LST product archived at the Meteorological and Oceanographic Satellite Data Archival Centre (MOSDAC), a specialized data center managed by the Space Applications Centre (SAC) of the Indian Space Research Organisation (ISRO) (53) (`https://mosdac.gov.in`). The LST product is derived from INSAT-3D/3DR, a series of Indian geostationary meteorological satellites operated by ISRO. The dataset represents the radiative skin temperature of the land surface, expressed in Kelvin, at a spatial resolution of approximately 0.1° and half-hourly temporal coverage. The difference between this LST

and the temperature recorded at the flux tower is referred to as the observed temperature difference (ΔT), used in the bulk parameterisation of SHF in the upcoming sections.

2.2 ERA5 Reanalysis Data

The observations were compared with values of the respective variables in the ERA5 reanalysis dataset for 2017. In addition to this, in order to evaluate the robustness of variability and trends in the reanalysis dataset, we present a decade-long analysis of ERA5 from 2014–2023. The ERA5 reanalysis dataset, developed by the European Centre for Medium-Range Weather Forecasts (ECMWF), is the successor to the widely used ERA-Interim product (54). ERA5 provides comprehensive global atmospheric, land-surface, and sea-state variables with enhanced spatiotemporal resolution. It offers hourly data at a horizontal resolution of approximately 31 km and includes 137 hybrid-sigma model levels extending from the surface up to 0.01 hPa. The dataset is generated using the Integrated Forecasting System (IFS), Cycle 41r2, which incorporates a 12-hour 4D-Var data assimilation scheme and variational bias correction to assimilate a wide range of satellite and in situ observations (55). ERA5 represents a significant advancement in reanalysis quality, with improved consistency, accuracy, and uncertainty estimates compared to its predecessor.

All analyses pertaining to the gridded ERA5 dataset have been performed at a single grid cell nearest to the flux tower site in Jaisalmer. Six single-level variables (56), namely temperature at 2 m (near-surface, short-name: `t2m`, unit: K), skin temperature (`skt`, K), surface sensible heat flux (`sshf`, J m^{-2}), and 10 m U and V wind components (`u10` and `v10`, m s^{-1}), and friction velocity (`zust`, m s^{-1}) were downloaded at a temporal frequency of 1 hour. One pressure-level variable namely, temperature at 1000 hPa was also downloaded at the same temporal frequency. All data are publicly available at the Copernicus Climate Data Store (57). Of these, the values for temperature at 2 m, skin temperature, and 10 m U and V wind components are instantaneous in time. The two wind variables were combined using vector addition to compute the total wind speed at 10 m. Unlike the aforementioned variables, surface sensible heat flux values were originally available as hourly accumulations. Moreover, as per the sign convention used by ERA5, the hourly accumulated fluxes are positive in the direction from the air downwards into the Earth's surface, and vice versa. For this analysis, these values were converted to mean flux per second (W m^{-2}) by scaling all values by $-1/3600$, reversing the sign convention so that fluxes into the land are represented with a negative sign in all subsequent sections.

2.3 Computing Obukhov Length

The Monin–Obukhov length is a key parameter in surface-layer similarity theory used to understand the relative importance of buoyancy and mechanical shear in generating turbulence.

$$L = -\frac{u_*^3\,\overline{\theta_v}}{\kappa g\,\overline{w'\theta_v'}}, \tag{3}$$

where u_* is the friction velocity, $\overline{\theta_v}$ is the mean virtual potential temperature, κ is the von Kármán constant (≈ 0.4), g is the acceleration due to gravity (9.81 m s^{-2}), and $\overline{w'\theta_v'}$ is the kinematic virtual potential temperature flux. A smaller magnitude of L implies a stronger buoyant influence, whereas a large $|L|$ indicates turbulence mainly governed by shear. Negative values of L indicate unstable or convective conditions where buoyancy enhances turbulence, positive values indicate stable conditions where buoyancy suppresses turbulence, and $|L| \to \infty$ corresponds to neutral conditions dominated by mechanical shear.

Due to the lack of humidity observations, the specific humidity was assumed to be zero, so that the virtual potential temperature θ_v reduces to the potential temperature θ, and the virtual temperature

flux $\overline{w'\theta'_v}$ reduces to kinematic sensible heat flux $\overline{w'\theta'}$. The potential temperature was computed from the measured temperature T and pressure p using

$$\theta = T\left(\frac{p_0}{p}\right)^{R/c_p}, \tag{4}$$

where $p_0 = 1000$ hPa is the reference pressure, R_d is the gas constant for dry air, and c_p is the specific heat capacity of dry air at constant pressure. The dynamic sensible heat flux (SHF, in $\mathrm{W\,m^{-2}}$) as in the observational data were converted to kinematic form using

$$\overline{w'\theta'} = \frac{\mathrm{SHF}}{\rho c_p}. \tag{5}$$

Combining these relations gives

$$L = -\frac{u_*^3\,\overline{\theta}}{\kappa g\,\overline{w'\theta'}}, \qquad \text{where} \quad u_* = \sqrt{\frac{\tau}{\rho}}. \tag{6}$$

For the computation of the Obukhov length (L, m), the potential temperature (θ, K) was derived from the ERA5 air temperature at 1000 hPa, which served as the reference pressure (P_0).

2.4 Computing wind speed ramps

The variability of low-level winds and the skill of ERA5 in its emulation were assessed systematically in several steps, such as comparing their annual and diurnal cycles and the patterns in change of wind speed. A wind ramp is defined as the change in wind speed over a certain duration (58), (59). The flow chart in Figure 1 describes our methodology in computing wind ramps and identifying regimes in their magnitude, duration, likelihood of occurrence during different phases of the diurnal cycle, and any seasonal variations in these features.

The results pertaining to each of these steps are presented in the following sections. The codes for the analyses performed on the datasets can be accessed in this GitHub repository.

3 Results

3.1 Annual and diurnal variability of variables

We begin by visualizing the observed seasonal and diurnal variability in near-surface air temperature, horizontal wind speed, and sensible heat flux at the surface at Jaisalmer during 2017 and comparing them with the corresponding ERA5 reanalysis values. Figure 2 shows the annual range of values of each of the three variables in ERA5 from 2014–2023 for robustness and compares it with the observed ranges during 2017. The annual range of observed near-surface temperature values during 2017 goes from 273.9–320.3 K with the inter-quartile range (IQR) between 295–308 K and the median being at 302 K (Figure 2b). The distribution is right-skewed. In the ERA5 dataset, the annual range during 2017 is between 277.8–319.3 K and the IQR between 294–307 K, while the median is at 301 K. Although ERA5 gets the median and the IQR nearly correct, it fails to simulate the lower extreme, thus underestimating the skewness in the distribution. The disparity in the lower limits of the two datasets may be attributed partially to the coarser temporal resolution of ERA5, which may smoothen out short-term variability captured in the higher-resolution observations (15 minutes). Throughout the decade, the median annual temperature as simulated in ERA5 is ∼301 K while the IQR and the annual extremes vary. Nonetheless, all distributions are right-skewed.

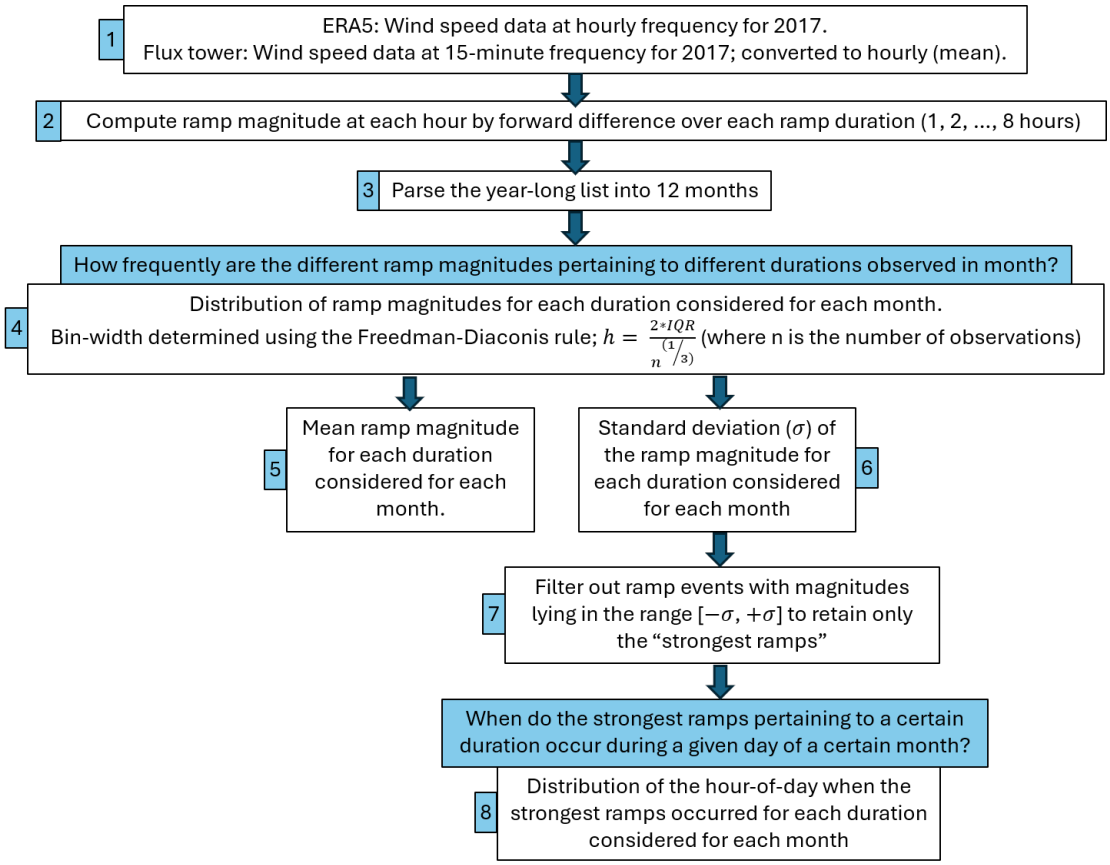

Figure 1: Analysis for wind ramps.

The distributions for wind speed at 10 m as simulated in ERA5 are left-skewed with long tails on the right throughout the decade including 2017. Across all years, the median remains close to 3.5 m s^{-1} and the IQR well within 2.5–5.2 m s^{-1}, while the higher extreme values vary between 12–15 m s^{-1} determining the tailedness of the distribution. Contrastingly, the observations recorded in 2017 have a much lower median of ∼2.3 m s^{-1} and a shorter IQR between 1.5–3.7 m s^{-1} (Figure 2d), indicating non-systematic overestimations by ERA5. The sensible heat flux observed at the surface during 2017 ranges from -169–610 W m^{-2}, with the IQR being -8–109 W m^{-2} and the median nearly coinciding with the lower bound of the IQR at 0 W m^{-2}. The distribution is heavily skewed towards the left. While ERA5 successfully simulates this characteristic skewness, as well as the value of median and the IQR robustly throughout the decade, the annual range is highly misrepresented. Hourly averages in ERA5 during each year from 2014–2023 range strictly between -68.3–405 W m^{-2} indicating its inability to simulate extremes.

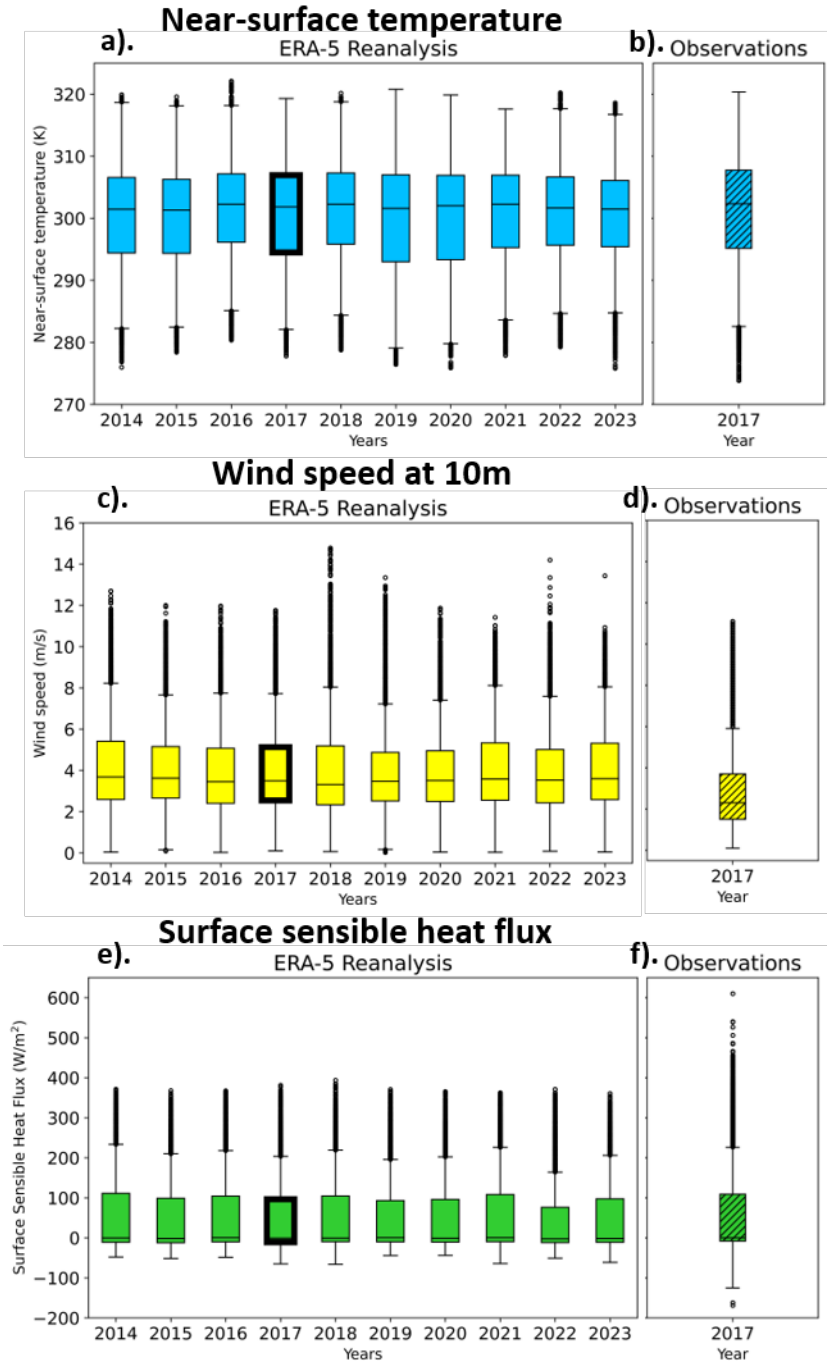

Figure 2: Boxplots representing the annual range of values for near-surface temperature (K) (a, b), wind speed at 10 m (m s^{-1}) (c, d) and SHF (W m^{-2}) (e, f). The years are indicated along the x-axis, and the data used is ERA5 reanalysis (a, c, e) and observations (b, d, f) for the respective variables. The top and bottom edges of each box represent the 75th and 25th percentiles (inter-quartile range) of the distribution, respectively. The central line marks the median. The maximum length of the whiskers is extended up to 1.5 times of the IQR on both sides of the box, and the remaining extreme values are marked as outliers.

The intra-annual variability in the above-mentioned variables is visualized using daily averages in order to neglect the diurnal variation which has been studied separately later. This observed daily average in 2017 is the lowest during December with values as low as 283 K that rises and peaks at

310 K during June. Following this increase, it gradually decreases during the local summer-monsoon season from June to September and then more rapidly between September and December. In addition to this, variations on a sub-monthly scale during winter may be attributed to the passage of synoptic systems such as western disturbances (60). Qualitatively, this interseasonal and subseasonal variability is seen to be well represented in ERA5 during 2017 (Figure 3a). However, despite capturing the qualitative pattern well, ERA5 exhibits notable deviations in magnitude, with daily averages differing from observations by up to 5 K on certain days. The overall annual bias is -0.5 K. Similar to the near-surface temperature, the observed wind speed shows a seasonal pattern. Although highly fluctuating on shorter temporal scales, low-level wind speed is observed to gradually increase from winter to summer, gaining the highest values of about 9–10 m s^{-1} around the local monsoon season, after which it drops again to values between 2–4 m s^{-1} (Figure 3c). As signatures of active and break spells during the Indian summer monsoon, intraseasonal variations are observed to be highly pronounced between June and mid-August, with the average daily values fluctuating between 2 m s^{-1} and 10 m s^{-1} during this period. These fluctuations are well captured in ERA5. Throughout the year, the wind speed is highly overestimated by ERA5 with anomalies as high as 150% on some days and the overall annual bias being 1.1 m s^{-1} (Figure 3d).

The daily average surface sensible heat flux is observed to increase gradually from January and peak at ∼120 W m^{-2} during June, then oscillate sharply to values as low as 10 W m^{-2} between July and September, following which they decline gradually to attain the lowest values in December (blue solid line in Figure 3e). This seasonal variation is simulated well in ERA5 (red solid line in Figure 3e). The standard deviation of the daily mean values over a decade in ERA5 data is nearly negligible during the winter months but is very high during summer when the soil moisture content is increased due to the local monsoon season controlling a major fraction of the heat exchange between the land and the atmosphere happening in the form of the latent heat of evaporation of water. ERA5 computes erroneous values particularly during the local monsoon months with the anomalies being as high as 300%, whereas during the other months of the year, the values are slightly underestimated (Figure 3f). The mean annual is -6.8 W m^{-2}.

In order to assess the diurnal variability in the observed values of variables and the skill of ERA5 in simulating these values, we particularly select two months namely May and December. A large seasonal contrast in the local weather conditions is seen between these months at a semi-arid location like Jaisalmer. The boundary layer is typically deepest during premonsoon months such as May and shallowest during winter months such as December, representing two extremes of boundary layer dynamics. These contrasting conditions motivated our choice of months. The observed values of near-surface temperature and surface sensible heat flux follow a similar characteristic diurnal cycle in both seasons alike. The near-surface temperature is lowest during the night, starts increasing after sunrise, and continues to increase during daytime to reach its highest value at 316 K and 298 K in May and December respectively, and then decreases after sunset until the next sunrise. Diurnal values range between 303.1–316 K during May, and between 283.5–298 K during December (Figure 4a). Throughout the day, ERA5 underestimates the near-surface temperatures causing a negative bias of -0.7 K in May and -1.2 K December respectively. A notable feature in the diurnal variation in ERA5 is that the curve nearly flattens out between 15:00 and 18:00 hours invariably during both months. In the case of the surface sensible heat flux, both its magnitude and direction depend upon the time of day. During the night, when the land undergoes radiative cooling and the air above is warmer, the sensible heat flux is directed into the ground (negative) and shows only slight variations in magnitude. After sunrise, as the land heats up rapidly due to the incoming solar radiation, the direction of the sensible heat flux changes. It increases rapidly to a high positive value until afternoon (130 W m^{-2} in December and 300 W m^{-2} in May) and then drops until it again becomes negative after sunset (Figure 4e, f).

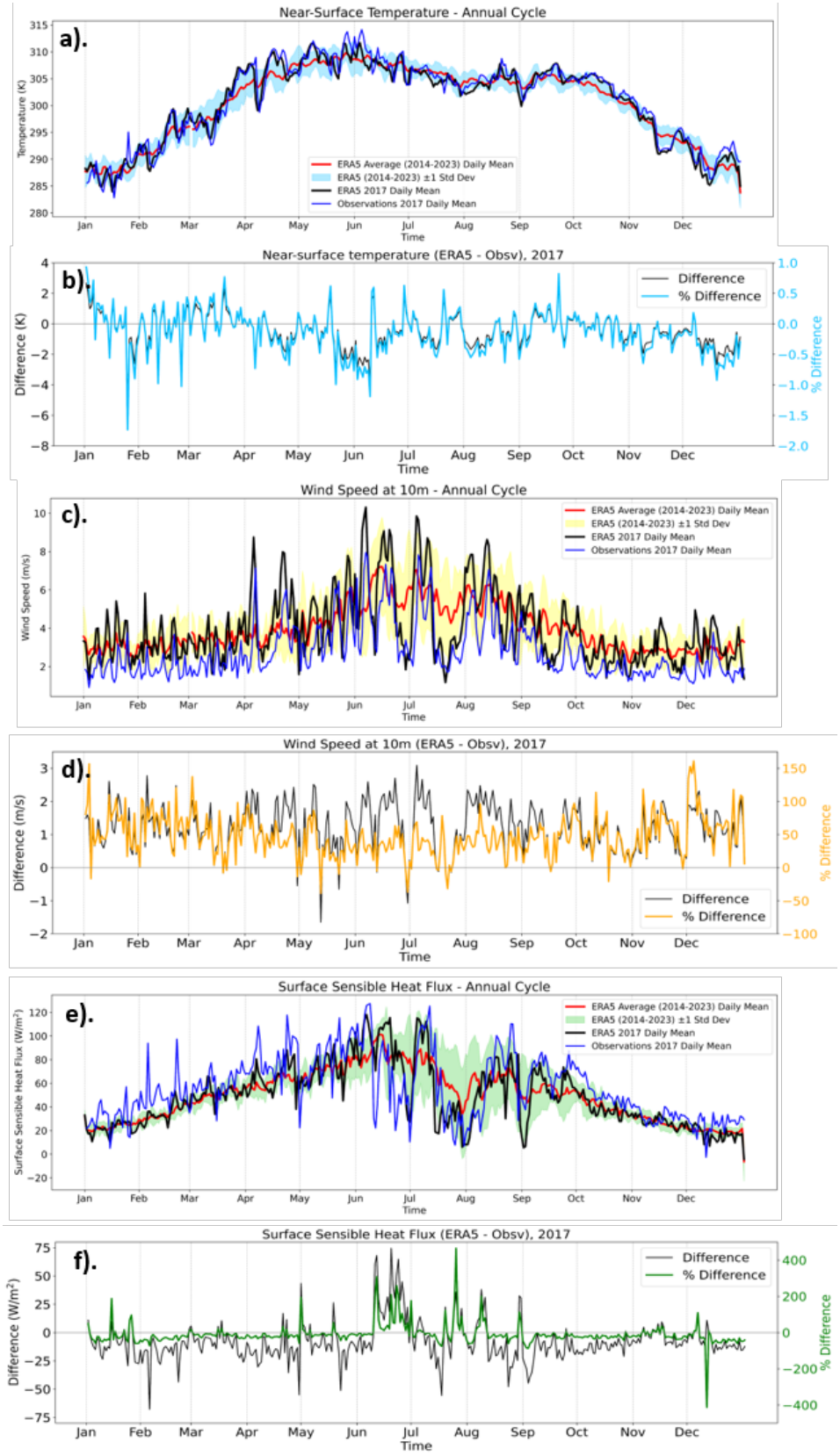

Figure 3: (a, c, e) Time series showing intra-annual variation in near-surface temperature (K), wind speed at 10 m (m s^{-1}) and SHF (W m^{-2}) respectively, in terms of ERA5 day-wise decadal average, first standard deviation, daily mean for 2017, and daily mean for 2017 for observations. (b, d, f) Time series for the error shown by ERA5 with respect to observations in the daily mean for 2017.

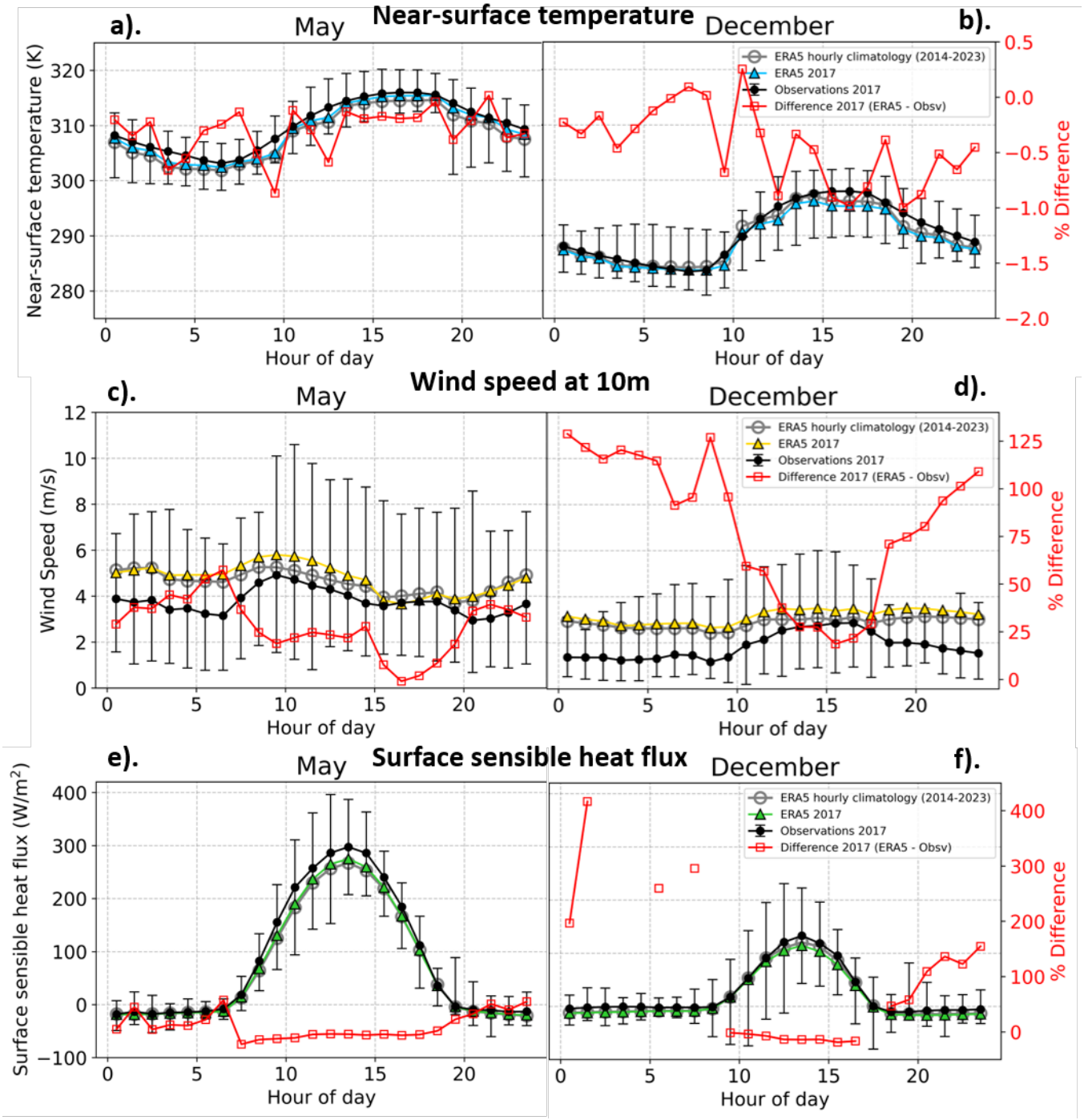

Figure 4: Diurnal variation in near-surface temperature (K) (a, b), wind speed at 10 m (m s^{-1}) (c, d), and SHF (W m^{-2}) (e, f) as seen in ERA5 reanalysis and observational data and their anomaly. We compare this between May (summer) (a, c, e) and December (winter) (b, d, f) for 2017. The difference axis (red) shows the bias of ERA5 with respect to observations. The error-bar in observations shows the hour-wise range of values over all days of the respective month.

We also observe that the hour-wise values through the month show greatest variability during the daytime hours and very low variability during nighttime, as can be inferred from the length of the range-bars in Figure 4e, f. ERA5 values differ significantly during the nighttime hours in December. In Figures 4e and f, the percent error of ERA5 computed with respect to the observational values blows up at certain points where the hourly mean of the measured SHF is close to zero. To circumvent

this, we considered a minimum threshold of 2 W m^{-2} for the observed SHF in order to compute the corresponding percent error seen in ERA5. The resultant daily bias of ERA5 with respect to observations is -7.8 W m^{-2} in May and -7.3 W m^{-2} in December.

Unlike SHF and the near-surface temperature, the low-level wind speed does not show a clear diurnal pattern. In general, observed wind speeds are higher during May (3–5 m s^{-1}) than in December (1–3 m s^{-1}) as has been stated previously while describing the seasonal variability of winds. ERA5 is seen to overestimate values at each hour resulting in an overall daily bias of 0.9 m s^{-1} in May and 1.3 m s^{-1} in December. Notably, the difference between ERA5 and the observed values is the least during the afternoon hours in both the months (∼3 pm in December and ∼4 pm in May) (Figure 4c, d).

3.2 Wind ramps at Jaisalmer

Although wind speeds do not show a striking diurnal cycle as can be inferred from the long variability whiskers in Figure 4c-d, an important feature of the mean diurnal plots for both May and December is a monotonic increase in wind speed during the morning hours. This begins earlier in the day and occurs much more rapidly during May (between 5 am and 10 am) than in December, when it is much more gradual and prolonged (10 am to 4 pm) (Figure 4c, d). This aspect, often referred to as ramps in wind speed, is crucial when it comes to evaluating and forecasting diurnal variation in wind power generation. Modern wind turbine designs are capable of generating electricity at relatively low wind speeds, with cut-in thresholds typically ranging between 3–4 m s^{-1}. Consequently, even under nearly calm conditions, an increase of approximately 3 m s^{-1} can initiate power production, highlighting the significance of such wind speed variations. In the following section we systematically analyse the wind ramps observed at Jaisalmer and the ability of ERA5 in capturing them.

We find that changes in wind speed within an hour go up to ∼4 m s^{-1} on some days in May but do not exceed ∼2.5 m s^{-1} in December. ERA5 largely underestimates ramps on a daily scale such that the ramp magnitude goes only up to 2 m s^{-1} on most days in May and up to 1 m s^{-1} on most days in December (Figure 5c, d). Interestingly, however, it does capture very well the hour-wise variation when averaged over a month, especially during May but also December (Figure 5e, f). This points towards a limitation of ERA5 in capturing diurnal variability in wind power generation on any given day, while still demonstrating reliability when applied at the monthly scale. This is true for all other months of the year (Figure 11).

In analyzing ramps of different durations, we computed the change in wind speed over a certain duration, and that value was assigned to the lower limit of the considered period. We learn that as we compute ramps over longer durations up to 8 hours, higher magnitudes become increasingly probable. This is an indicator of the cumulative growth of wind speed over that duration. Changes in wind speed over an hour go up to 2.5 m s^{-1}, but the cumulative ramp magnitude over durations as long as 8 hours does not exceed roughly 4.5 m s^{-1} as is clearly seen in Figure 6. The distribution of the cumulative change in wind speed over long durations shows very slight seasonal variations. We find that the highest ramp magnitudes occur during the summer and monsoon seasons, whereas those in winter are slightly lower. We have shown distributions for some representative months in Figure 6. The mean and mode of the observed wind ramps was found to be close to zero for all ramp durations. The contours on the heatmap indicate the frequency of ramp events derived using ERA5 data. They closely follow the distribution depicted by the heatmap in their qualitative form and orientations. The red lines in each row mark the $\pm 1\sigma$ of the distribution in that row.

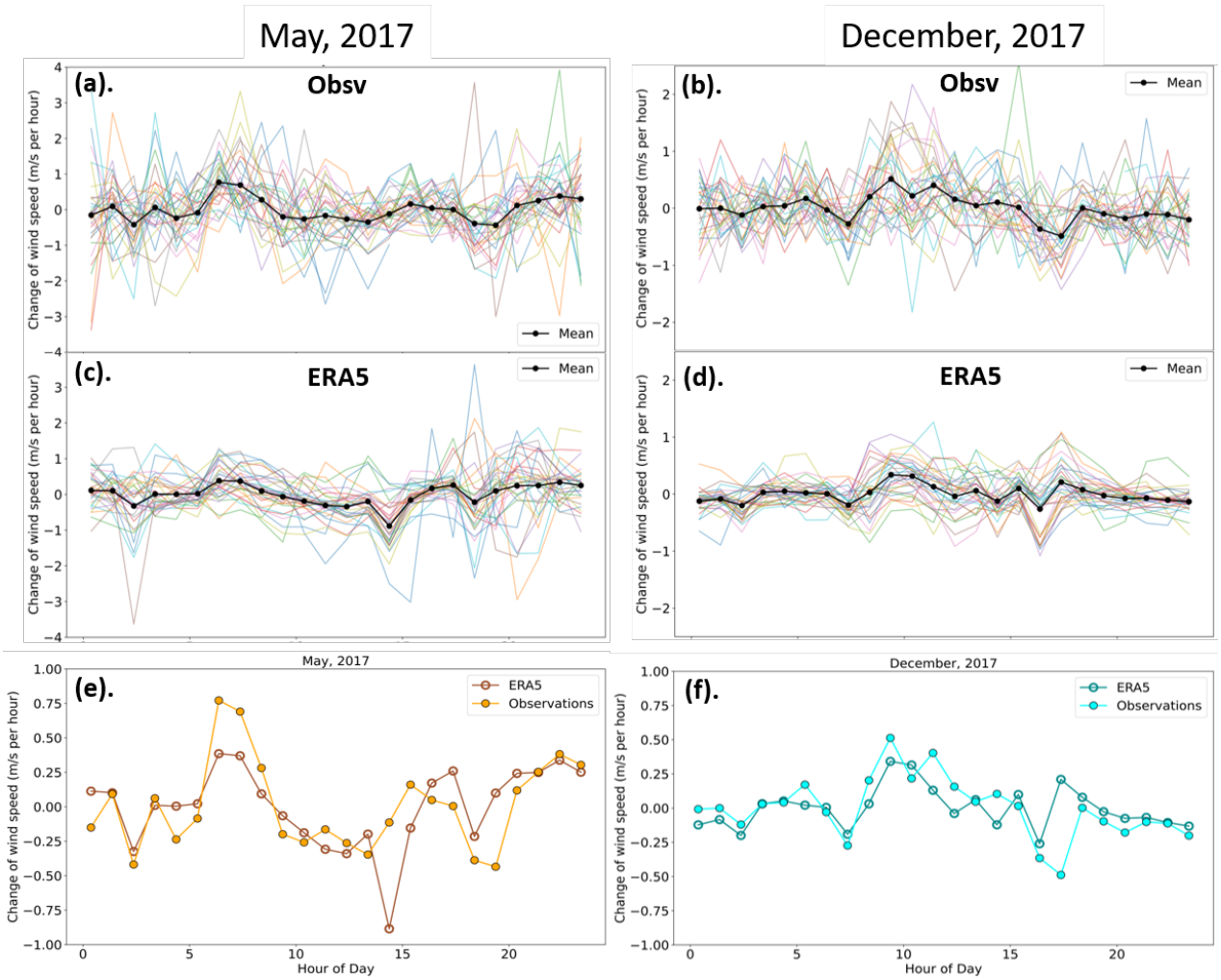

Figure 5: Diurnal variation in the rate of change of wind speed per hour for days in May (a, c) and December (b, d) as seen in the observational (a, b) and ERA5 (c, d) data. Each thin colored line represents one day (31 thin lines for both December and May respectively) and the thick black line is the hour-wise monthly mean. The hour-wise mean computed over observed and ERA5 values has been presented in sub-figures e (May) and f (December).

Having characterized the magnitudes of wind ramps occurring over different durations, we next assess whether these ramps preferentially occur during specific hours of the day. For this purpose, ramp events were filtered to retain only those with magnitudes greater than the ± 1 standard deviation. This range has also been mentioned in the far right margin of Figure 6. During the winter months of December (Figure 6d) and January, wind ramp events occur most frequently in the morning and late afternoon hours, indicating a distinct diurnal preference. In contrast, such a well-defined diurnal cycle is absent during the summer months, when the boundary layer is deeper and turbulence is predominantly buoyancy-driven. The absence of a distinct diurnal cycle extends through the onset phase of the monsoon and the early monsoon weeks of July, when boundary-layer dynamics remain strongly modulated by transient convective activity. In August, which coincides with the climatological peak of annual rainfall over Jaisalmer, a renewed well-defined diurnal pattern in ramp occurrence emerges. The number on each grid-cell in the heatmaps 6b, d, e shows the deviation of ERA5 from the observed value. Herein, the values in yellow represent positive deviations or over-estimations by ERA5 and those in white imply underestimations. An alternate occurrence of patches numbers as is very clearly apparent in the month of August (Figure 6f) means that ERA5 displaces the most preferred hour of wind ramp occurrence implying impending failure in short-term forecast of ramps.

For the sake of brevity, distributions for months other than May, August, and December have not been included in this section but can be found in the supplementary material (Figure 12, 13).

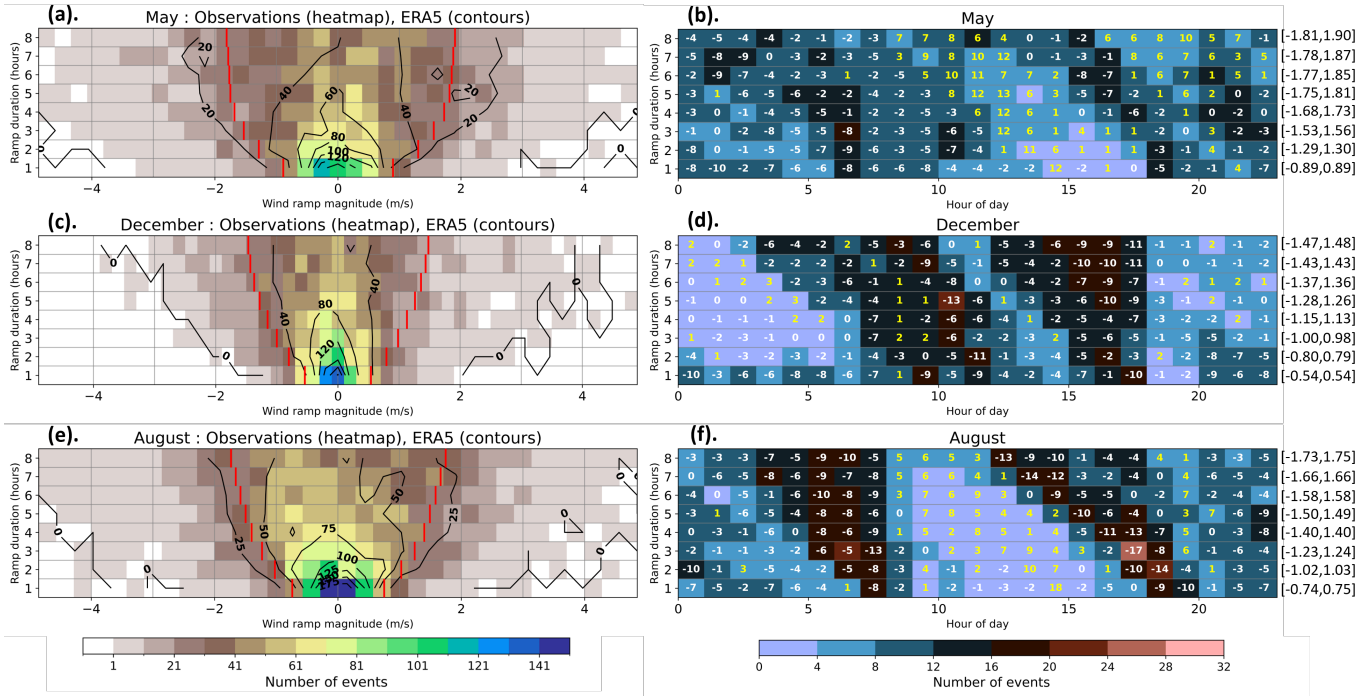

Figure 6: Heatmaps showing the frequency of occurrence of wind ramp events of durations ranging from 1-8 hours (along the ordinate) in (a) May, (c) December, (e) August as observed during 2017. The contours represent the corresponding values in ERA5. The red vertical segments in each row mark the ±1 standard deviation pertaining to the distribution in that row (also mentioned on the far right margin of the figure). (b, d, f) correspond to the diurnal occurrence of ramps with magnitudes outside the mentioned range. The number in each gridcell is the error shown by ERA5.

During certain periods of the day, distinct patches appear in the diurnal cycle where wind speed remains nearly steady and rapid fluctuations are suppressed. This pattern is most pronounced in December and January, when the diurnal periodicity in wind ramp occurrence is well defined. This strengthened our motivation to examine the relationship between low-level wind speed and surface sensible heat flux to assess whether the absence of ramps is associated with particular surface–atmosphere coupling regimes or thermodynamic controls.

3.3 Bulk parameterization of SHF

We find that the low-level wind speed at night scales linearly with the sensible heat flux directed into the ground (Figure 7), particularly during December and January, when the boundary layer is extremely stable and the temperature inversion is pronounced. This linear relationship is not evident at shorter time scales, such as 2-hour intervals (Figure 9), but becomes apparent when the coefficient of determination (R^2) is computed over longer periods of approximately 12 hours (i.e., from 6 pm to 6 am). ERA5 shows a stronger correlation than the observations, yielding an R^2 value of 0.69 compared to 0.54. A notable feature of this relationship is that it manifests only above a certain wind speed threshold ($\sim$ 1.2 $\mathrm{m\,s^{-1}}$ in December), below which the sensible heat flux remains nearly invariable. ERA5 overestimates this threshold to $\sim$ 1.8 $\mathrm{m\,s^{-1}}$. Such a linear relationship is largely absent during summer, when the nighttime inversion is comparatively weaker. Figure 8 illustrates the intra-annual variability in characteristics of the nighttime regime, namely the coefficient of determination, slope, and

intercept, revealing a clear seasonal trend. While the linear relationship is strongest during the winter months of December and January, it gradually weakens as summer approaches, and disappears in June, before re-emerging in winter. ERA5 fails to capture this gradual seasonal transition, instead exhibiting a more abrupt and "jumpy" distinction between summer and winter. Moreover, ERA5 fails to capture the correct seasonal timing as it shows the strongest nighttime correlations in March and October, whereas the observations show they actually occur in December and January. The anomalously strong linear relationship in October disrupts the expected seasonal gradient. In months with considerably high R^2 values, the negative slope predicted by ERA5 is much steeper, and the threshold wind speed higher.

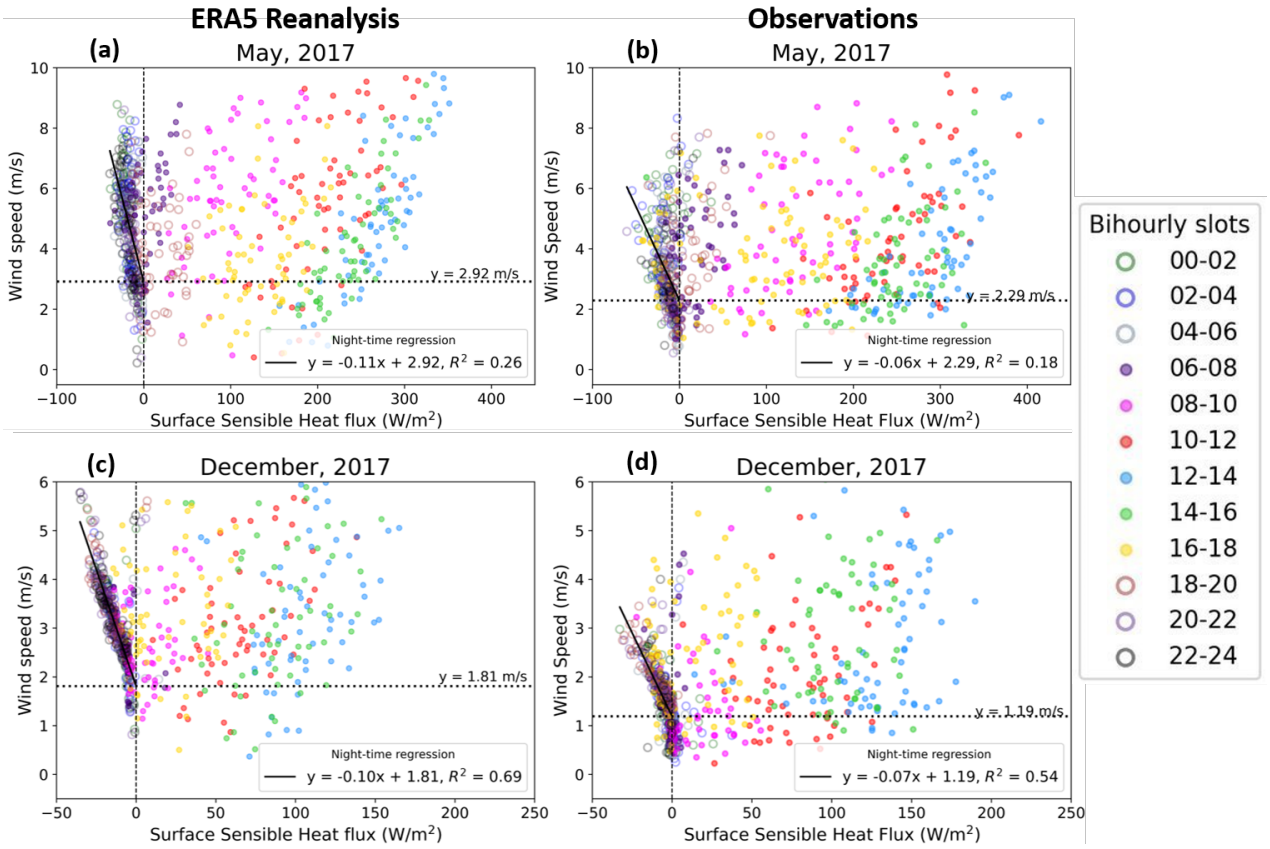

Figure 7: Comparison of scatters between SHF (W m^{-2}) and wind speed (m s^{-1}) for the months of May (summer) (a, b) and December (winter) (c, d) in 2017 using ERA5 reanalysis (a, c) and observational (b, d) data respectively. The points have been colored as per the hour of day, and also differentiated between nighttime (defined as 6 pm to 6 am) and daytime (6 am to 6 pm) using open and closed circles respectively. The black solid lines are the linear fits for points during the nighttime with SHF < 0.

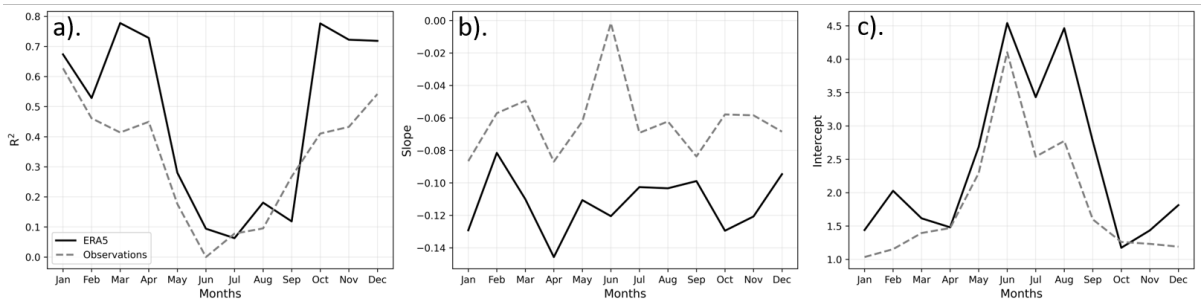

Figure 8: Summarizing the metrics of the linear regression between SHF and wind speed for nighttime hours (coefficient of determination (a), slope (b) and intercept / wind speed threshold (c)) for all months of 2017 using ERA5 reanalysis and observations.

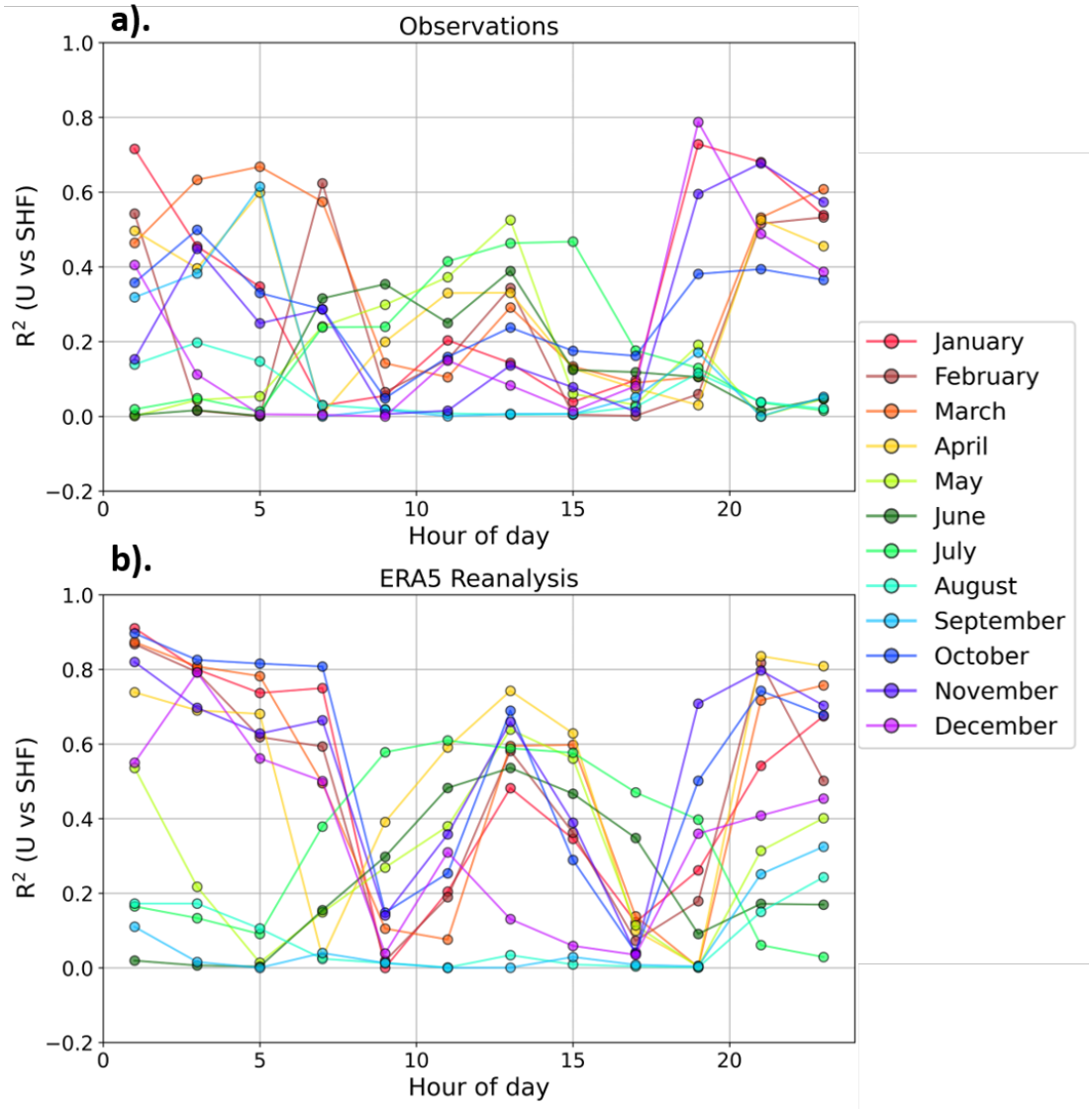

Figure 9: Monthwise diurnal variation in the coefficient of determination corresponding to a linear regression between the surface sensible heat flux and wind speed in 2 hour-long slots using a). observational data and b). ERA5 reanalysis during 2017.

In addition to the night-time regime observed during winter, we also identified a day-time regime occurring in the summer months, specifically May. During peak afternoon hours, sensible heat flux and wind speed exhibit a linear relationship. Visually, this appears as a distinct band of scatter points corresponding to the time slots 12–2 pm and 2–4 pm in the Figure 7a, b. This regime is much shorter in duration compared to the longer-lasting night-time regime. A contrasting seasonality is evident, where the daytime regime reaches its peak in May and is largely absent in other months. In some months, negative R^2 values are observed during the said time slots. ERA5 overestimates the day-time linear relationship in May and also shows erroneously high correlations during the winter months, failing to capture the correct seasonal trends.

Figure 9 shows the month-wise diurnal variation of the coefficient of determination (R^2) between surface sensible heat flux and low-level wind speed, computed over 2-hour intervals. Panel (a) corresponds to the observations, and panel (b) to ERA5 reanalysis particularly during 2017. In the observations, the diurnal evolution of R^2 exhibits a clear seasonal dependence, with distinct nighttime and daytime regimes. The winter months exhibit a concave diurnal structure, with the highest correlations occurring at night, when the boundary layer is stably stratified, and reduced R^2 during daylight hours when wind–flux coupling is weakest. As the year progresses toward summer, this concavity gradually transitions to a convex shape, reflecting the dominance of the daytime regime during afternoon hours (12–4 pm local time), when strong surface heating drives turbulence and enhances wind–flux coupling. Intermediate months display transitional shapes, with both regimes contributing to the overall diurnal pattern. ERA5 reproduces some aspects of the observed diurnal variability but with notable discrepancies. While it correctly suggests a stronger relationship during the night, particularly in winter, the R^2 values are generally higher than in the observations across most months and hours, frequently exceeding 0.8 during the winter nighttime. Critically, March and October are incorrectly simulated as having one of the strongest nighttime correlations, with R^2 values approaching 0.9. The distinct concave shape in winter is not captured; instead, a persistent midday peak is evident in almost all months, making the curves more uniform regardless of season. The convexity during the summer months, however, is well represented. In addition, these month-wise diurnal cycles in ERA5 may be considered robust and not an artefact of 2017 in particular, as these patterns have been consistently reproduced throughout the entire decade from 2014 to 2023 (Figure 14).

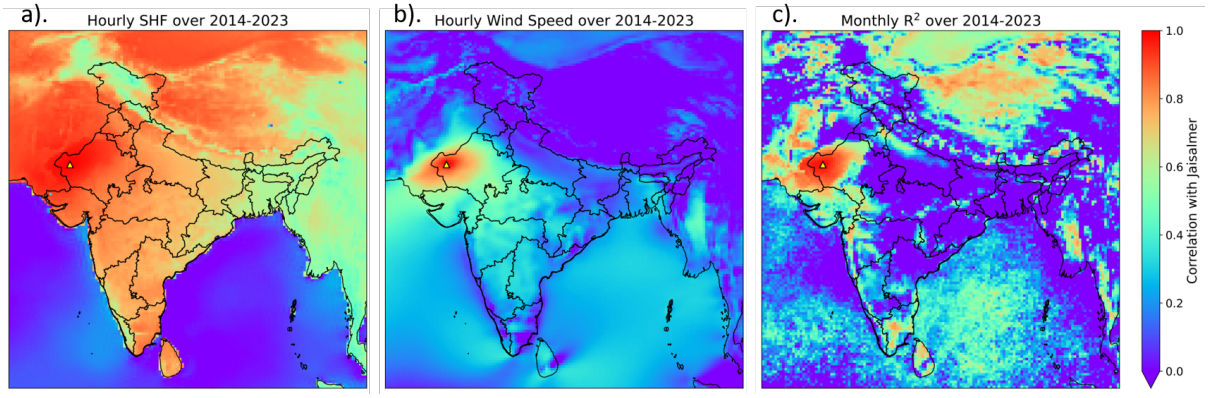

Figure 10: Spatial correlation with Jaisalmer for (a) SHF, (b). U, (c). R2 between U and SHF. Triangle in yellow represents the location of Jaisalmer.

4 Summary and Discussion

In this study, we began by evaluating the values of three variables: near-surface wind speed ($\sim 8\,m$), near-surface air temperature ($\sim 8\,m$), and the surface sensible heat flux observed at a flux tower in

Jaisalmer as part of the INCOMPASS field campaign during 2017. The observed magnitude ranges, as well as the annual and diurnal variations in each variable, were compared with their analogues in the ERA5 reanalysis data (horizontal wind speed at 10 m, temperature at 2 m, and the surface sensible heat flux) in order to evaluate the skill of the reanalysis dataset in reproducing the observations at Jaisalmer. In particular, the comparison of diurnal cycles was done separately for May and December, considering the stark seasonal differences at a semi-arid location like Jaisalmer. To assess the consistency in trends seen in ERA5, we considered a ten-year period of ERA5 data (2014–2023), centered around the year 2017 for which observational data was available.

We learnt that the median and IQR of near-surface temperature and SHF in ERA5 were robust across years and matched well with observations. While ERA5 also captured the overall range for temperature, it failed to capture the extreme negative and positive SHF values seen in the observations. This may be partly attributed to the mismatch in temporal resolution of the two datasets (hourly in ERA5 versus 15 minutes in observations). On the other hand, for wind speed, ERA5 captured the extreme magnitudes and overall range, but the median and IQR were substantially overestimated compared to observations. This bias persisted across the entire decade in ERA5, and annual variability comparisons also showed daily mean wind speed errors reaching up to 150%. Wind speed exhibited strong oscillations throughout the year, particularly from June to August during the local monsoon season, which was also when ERA5 showed the highest interannual variability. Near-surface temperature followed a clear annual cycle with the lowest extremes occurring in December and January, rising steadily to peak in June, decreasing through September, increasing slightly in October, and declining again toward winter. ERA5 reproduced this pattern well, although at some instances the daily means differed by -8 to $4\,K$. SHF showed an analogous annual cycle such that it was lowest in December and January, increased steadily to reach its maximum in June, and exhibited a sharp dip in August which is climatologically known to be the month of highest annual precipitation, likely due to enhanced soil moisture and the resulting dominance of latent heat flux over sensible heat flux. It rose again in September and decreased toward winter. Characteristic diurnal cycles were evident for temperature and SHF, but not for wind speed. In both May and December, SHF peaked around 1 pm; however, December exhibited high negative SHF values after the local sunrise, extending into late morning hours (9–11 am) and just before sunset, whereas in May negative values occurred only during nighttime hours (i.e., after sunset and prior to sunrise). Near-surface temperature began to rise around 6:30 am in May and 8:30 am in December due to the later sunrise, and began to decline much earlier in December. The temperature difference between the two months was approximately $20\,K$ at all hours. Wind speeds were generally higher and showed more variation in May than in December, with a characteristic pickup in wind speed during the morning hours in both months. These qualitative patterns were faithfully captured in ERA5, providing confidence to proceed with more detailed and non-trivial comparisons between the two datasets. Given the growing technological importance of Jaisalmer as a wind energy hub, we proceeded to compare more nuanced characteristics such as the occurrence of wind speed ramps and the coupling of low-level wind speed with the sensible heat flux at the surface.

Despite the absence of a strict diurnal cycle in wind speed, its gradual rise during the morning hours in both May and December motivated a detailed evaluation of ramps in low-level horizontal wind speed over Jaisalmer. Hourly ramps were observed to be much stronger during May (when the overall wind speed was also higher, as discussed previously) (up to $4\,\mathrm{m\,s^{-1}}$) than in December (up to $2\,\mathrm{m\,s^{-1}}$). ERA5 does not capture this variability on an hourly scale. However, the monthly average diurnal cycle of wind ramp magnitudes in ERA5 is highly comparable to that computed using flux-tower observations implying the usability of ERA5 in forecasting average diurnal variability in wind power potential over monthly time scales. Wind speed at lower levels is related to that at higher elevations, such as the 100 m hub height, through power-law or logarithmic relationships that depend on local conditions. Consequently, wind ramps that occur near the surface can translate into corresponding changes at hub height. Accurate modelling of wind ramps is essential for forecasting wind power generation, as wind

power potential is proportional to the cube of the horizontal wind speed (61), and rapid changes in wind speed can also influence turbine efficiency.

$$P = \frac{1}{2}\rho A U^3 \tag{7}$$

where P is the wind power potential (W), ρ is the air density ($\mathrm{kg\,m^{-3}}$), A is the swept area of the turbine blades ($\mathrm{m^2}$), and U is the horizontal wind speed ($\mathrm{m\,s^{-1}}$). Analysis of wind ramps of different durations (ranging from 1 to 8 hours) revealed that the strongest ramps over Jaisalmer do not exceed a magnitude of 4 m $\mathrm{s^{-1}}$ and occur during the summer months. During winter, the occurrence of wind ramps shows a clear diurnal cycle with the morning and late afternoon hours experiencing the highest number of wind ramp events. This distinct diurnal pattern is absent in the other months but re-emerges strongly only during August, which is also a month experiencing a significant dip in SHF as its value becomes comparable to that during the winter months. This characteristic month-wise diurnal cycle in occurrence of wind ramps is represented poorly in ERA5.

Interestingly, the period of no wind ramps in winter coincides well with the night-time during which the low-level wind speed and the sensible heat flux directed into the land are linearly related. During the winter months, particularly in December and January, the nocturnal sensible heat flux directed into the land surface exhibits a near-linear scaling with low-level wind speed once a critical threshold of approximately 1–1.2 m $\mathrm{s^{-1}}$ is exceeded. This regime progressively weakens and disappears in the summer season. In contrast, during summer, a comparable linear relationship is observed only for a brief interval between 12 pm to 4 pm IST.

Heat exchange in the boundary layer may be thought of as a combination of three simultaneously occurring interdependent processes namely, the exchange between the surface and the lowest layer of the atmosphere (SHF), vertical mixing of this heat in the mixed layer through turbulence processes, and the horizontal advection of heat by background winds in response to spatial gradients. Unique balances between these processes and their competing rates may explain the distinct regimes that we observed. The temporal scale of each regime would be determined by the rate associated with the slowest process.

During winter nights, strong radiative cooling of the surface establishes a highly stable boundary layer with a pronounced temperature inversion and a consequent absence of buoyancy-driven turbulence. Mechanically forced turbulence becomes the dominant mechanism for vertical mixing of air parcels. Shear-generated eddies intermittently transport warmer air parcels to lower atmospheric levels that are colder by virtue of their proximity to the ground. This transport of warm air parcels enables sensible heat transfer into the surface in the presence of a temperature gradient established as a result of the radiative cooling. This establishes a one-to-one relationship between the wind speed (causing mechanical turbulence) and heat flux directed into the ground. When the wind speed is low, shear-driven turbulence is not efficient enough to facilitate a downward transfer of warm parcels, which explains the threshold in wind speed below which SHF is unresponsive to any changes in it. The rate of turbulent transport through vertical mixing exceeds that of the evolving temperature gradient between the land and near-surface air caused by radiative cooling, such that the latter constrains the pace of the overall flux magnitude. Thus, while wind speed primarily governs the magnitude of the sensible heat flux into the ground, the time scale of this regime is controlled by the rate of change of the temperature difference, a combination of radiative cooling and sensible heating.

Contrastingly, during summer afternoons, high positive SHF causes vigorous convection which along with the contribution from shear-driven turbulence gives rise to a highly efficient mechanism for vertical mixing. Jaisalmer being at the far northwestern end of the Indian summer monsoon trough, the summer months of May and June are characterized by peak seasonal heat and dryness, eliminating the possibility of any losses in the form of the latent heat of vaporization of water. Moreover, the

rate of change of SHF is also the least as it peaks during this period (Figure 4e). Rapid and efficient vertical heat transfer implies that turbulent mixing time scales become shorter compared to those of horizontal advection and SHF at the surface. This leads to a coupling between SHF and near-surface wind, producing the observed daytime linear scaling for a brief period during which this balance is non-transient and persistent.

In order to substantiate these hypotheses and better understand the underlying mechanisms, detailed large-eddy simulation (LES) experiments will be required. Unlike conventional LES studies wherein a fixed surface sensible heat flux is prescribed, such simulations should allow the surface flux to respond interactively to the evolving thermodynamic and dynamical state of the boundary layer. This would enable a more realistic representation of how SHF co-evolves with varying stability regimes, background wind conditions, and turbulence structures. This framework may further help explain the discrepancies in ERA5, which arise from its parameterized representation of these processes, particularly during the afternoon unstable boundary layers.

References

[1] Tariq Umar and Charles Egbu. Global commitment towards sustainable energy. *Proceedings of the Institution of Civil Engineers - Engineering Sustainability*, 172:315–323, 9 2019. doi:10.1680/jensu.17.00059.

[2] Neeraj Golait, R.M. Moharil, and P.S. Kulkarni. Wind electric power in the world and perspectives of its development in india. *Renewable and Sustainable Energy Reviews*, 13:233–247, 1 2009. doi:10.1016/j.rser.2007.07.005.

[3] Prem Kumar Chaurasiya, Vilas Warudkar, and Siraj Ahmed. Wind energy development and policy in india: A review. *Energy Strategy Reviews*, 24:342–357, 4 2019. doi:10.1016/j.esr.2019.04.010.

[4] A. K. Singh and S. K. Parida. Evaluation of current status and future directions of wind energy in india. *Clean Technologies and Environmental Policy*, 15:643–655, 8 2013. doi:10.1007/s10098-012-0554-6.

[5] J Charles Rajesh Kumar, D Vinod Kumar, D Baskar, B Mary Arunsi, R Jenova, and MA Majid. Offshore wind energy status, challenges, opportunities, environmental impacts, occupational health, and safety management in india. *Energy & Environment*, 32:565–603, 6 2021. doi:10.1177/0958305X20946483.

[6] M. Carolin Mabel and E. Fernandez. Growth and future trends of wind energy in india. *Renewable and Sustainable Energy Reviews*, 12(6):1745–1757, 8 2008. doi:10.1016/j.rser.2007.01.016.

[7] Upma Singh, Mohammad Rizwan, Hasmat Malik, and Fausto Pedro García Márquez. Wind energy scenario, success and initiatives towards renewable energy in india—a review. *Energies*, 15(6):2291, 3 2022. doi:10.3390/en15062291.

[8] Jami Hossain, Vinay Sinha, and V.V.N. Kishore. A gis based assessment of potential for windfarms in india. *Renewable Energy*, 36(12):3257–3267, 12 2011. doi:10.1016/j.renene.2011.04.017.

[9] A.K. Jaswal and A.L. Koppar. Climatology and trends in near-surface wind speed over india during 1961–2008. *Mausam*, 64(3):417–436, 7 2013. doi:10.54302/mausam.v64i3.725.

[10] Atul Sharma, Jaya Srivastava, Sanjay Kumar Kar, and Anil Kumar. Wind energy status in india: A short review. *Renewable and Sustainable Energy Reviews*, 16(2):1157–1164, 2 2012. doi:10.1016/j.rser.2011.11.018.

[11] Joseph P. Hennessey. Some aspects of wind power statistics. *Journal of Applied Meteorology (1962-1982)*, 16(2):119–128, 1977. URL: http://www.jstor.org/stable/26178141.

[12] Bharat Kumar Saxena and K.V.S. Rao. Estimation of wind power density at a wind farm site located in western rajasthan region of india. *Procedia Technology*, 24:492–498, 2016. doi:10.1016/j.protcy.2016.05.084.

[13] Mohammad Mohsin and K.V.S. Rao. Estimation of weibull distribution parameters and wind power density for wind farm site at akal at jaisalmer in rajasthan. In *2018 3rd International Innovative Applications of Computational Intelligence on Power, Energy and Controls with their Impact on Humanity (CIPECH)*, pages 1–6. IEEE, 11 2018. doi:10.1109/CIPECH.2018.8724170.

[14] Sakshi Shukla, Rohit Ramaprasad, Sumanta Pasari, and Sarita Sheoran. Statistical analysis and forecasting of wind speed. In *2022 4th International Conference on Energy, Power and Environment (ICEPE)*, pages 1–6. IEEE, 4 2022. doi:10.1109/ICEPE55035.2022.9798358.

[15] B. N. VISHNOI and VIRENDRA SINGH. Wind analysis for wind power at jaisalmer. *MAUSAM*, 56:904–907, 10 2005. doi:10.54302/mausam.v56i4.1087.

[16] Kurian J. Vachaparambil, Eric Aby Philips, Karan Issar, Vaidehi Parab, Divya Bahadur, and Sat Gosh. Optimal siting considerations for proposed and extant wind farms in india. *Energy Procedia*, 52:48–58, 2014. doi:10.1016/j.egypro.2014.07.053.

[17] T.N. JHA, K. C. SINHA RAY, and H. N. SRIVASTAVA. Coupling and decoupling processes in monsoonal surface layer using montblex-90 tower data. *MAUSAM*, 48:375–384, 7 1997. doi:10.54302/mausam.v48i3.4266.

[18] Kusuma G. Rao, R. Narasimha, and A. Prabhu. An analysis of montblex data on heat and momentum flux at jodhpur. *Journal of Earth System Science*, 105:309–323, 9 1996. doi:10.1007/BF02841885.

[19] Kusuma G. Rao, R. Narasimha, and A. Prabhu. Estimation of drag coefficient at low wind speeds over the monsoon trough land region during montblex-90. *Geophysical Research Letters*, 23:2617–2620, 9 1996. doi:10.1029/96GL02368.

[20] A. G. Turner, G. S. Bhat, G. M. Martin, D. J. Parker, C. M. Taylor, A. K. Mitra, S. N. Tripathi, S. Milton, E. N. Rajagopal, J. G. Evans, R. Morrison, S. Pattnaik, M. Sekhar, B. K. Bhattacharya, R. Madan, Mrudula Govindankutty, J. K. Fletcher, P. D. Willetts, A. Menon, J. H. Marsham, K. M. R. Hunt, T. Chakraborty, G. George, M. Krishnan, C. Sarangi, D. Belušić, L. Garcia-Carreras, M. Brooks, S. Webster, J. K. Brooke, C. Fox, R. C. Harlow, J. M. Langridge, A. Jayakumar, S. J. Böing, O. Halliday, J. Bowles, J. Kent, D. O'Sullivan, A. Wilson, C. Woods, S. Rogers, R. Smout-Day, D. Tiddeman, D. Desai, R. Nigam, S. Paleri, A. Sattar, M. Smith, D. Anderson, S. Bauguitte, R. Carling, C. Chan, S. Devereau, G. Gratton, D. MacLeod, G. Nott, M. Pickering, H. Price, S. Rastall, C. Reed, J. Trembath, A. Woolley, A. Volonté, and B. New. Interaction of convective organization with monsoon precipitation, atmosphere, surface and sea: The 2016 incompass field campaign in india. *Quarterly Journal of the Royal Meteorological Society*, 146:2828–2852, 7 2020. doi:10.1002/qj.3633.

[21] Dennis Baldocchi, Eva Falge, Lianhong Gu, Richard Olson, David Hollinger, Steve Running, Peter Anthoni, Ch Bernhofer, Kenneth Davis, Robert Evans, et al. Fluxnet: A new tool to study the temporal and spatial variability of ecosystem-scale carbon dioxide, water vapor, and energy flux densities. *Bulletin of the American Meteorological society*, 82(11):2415–2434, 2001.

[22] Jason P. Horne, Scott J. Richardson, Samantha L. Murphy, Helen C. Kenion, Bernd J. Haupt, Benjamin J. Ahlswede, Natasha L. Miles, and Kenneth J. Davis. Urban eddy covariance – the influx network, 6 2025. doi:10.5194/essd-2025-232.

[23] T. Murakami. Scientific objectives of the monsoon experiment (monex). *GeoJournal*, 3, 1979. doi:10.1007/BF00257701.

[24] Gregory S Poulos, William Blumen, David C Fritts, Julie K Lundquist, Jielun Sun, Sean P Burns, Carmen Nappo, Robert Banta, Rob Newsom, Joan Cuxart, et al. Cases-99: A comprehensive investigation of the stable nocturnal boundary layer. *Bulletin of the American Meteorological Society*, 83(4):555–582, 2002.

[25] GARY J. KUNKEL and IVAN MARUSIC. Study of the near-wall-turbulent region of the high-reynolds-number boundary layer using an atmospheric flow. *Journal of Fluid Mechanics*, 548:375–402, 2 2006. doi:10.1017/S0022112005007780.

[26] Kusuma G. Rao. Estimation of the exchange coefficient of heat during low wind convective conditions. *Boundary-Layer Meteorology*, 111:247–273, 5 2004. doi:10.1023/B:BOUN.0000016495.85528.d7.

[27] KUSUMA G. RAO and R. NARASIMHA. Heat-flux scaling for weakly forced turbulent convection in the atmosphere. *Journal of Fluid Mechanics*, 547:115–135, 1 2006. doi:10.1017/S0022112005007251.

[28] Iain Staffell and Stefan Pfenninger. Using bias-corrected reanalysis to simulate current and future wind power output. *Energy*, 114:1224–1239, 11 2016. doi:10.1016/j.energy.2016.08.068.

[29] Liam Hayes, Matthew Stocks, and Andrew Blakers. Accurate long-term power generation model for offshore wind farms in europe using era5 reanalysis. *Energy*, 229:120603, 8 2021. doi:10.1016/j.energy.2021.120603.

[30] Jon Olauson. Era5: The new champion of wind power modelling? *Renewable Energy*, 126:322–331, 10 2018. doi:10.1016/j.renene.2018.03.056.

[31] Sai Krishna V.S. Sakuru and M.V. Ramana. Wind power potential over india using the era5 reanalysis. *Sustainable Energy Technologies and Assessments*, 56:103038, 3 2023. doi:10.1016/j.seta.2023.103038.

[32] China Satyanarayana Gubbala, Venkata Bhaskar Rao Dodla, and Srinivas Desamsetti. Assessment of wind energy potential over india using high-resolution global reanalysis data. *Journal of Earth System Science*, 130:64, 6 2021. doi:10.1007/s12040-021-01557-7.

[33] Pedro M M Soares, Daniela C A Lima, and Miguel Nogueira. Global offshore wind energy resources using the new era-5 reanalysis. *Environmental Research Letters*, 15:1040a2, 10 2020. doi:10.1088/1748-9326/abb10d.

[34] Katharina Gruber, Peter Regner, Sebastian Wehrle, Marianne Zeyringer, and Johannes Schmidt. Towards global validation of wind power simulations: A multi-country assessment of wind power simulation from merra-2 and era-5 reanalyses bias-corrected with the global wind atlas. *Energy*, 238:121520, 1 2022. doi:10.1016/j.energy.2021.121520.

[35] G. Gualtieri. Analysing the uncertainties of reanalysis data used for wind resource assessment: A critical review. *Renewable and Sustainable Energy Reviews*, 167:112741, 10 2022. doi:10.1016/j.rser.2022.112741.

[36] Jaume Ramon, Llorenç Lledó, Verónica Torralba, Albert Soret, and Francisco J. Doblas-Reyes. What global reanalysis best represents near-surface winds? *Quarterly Journal of the Royal Meteorological Society*, 145:3236–3251, 10 2019. doi:10.1002/qj.3616.

[37] María O. Molina, Claudia Gutiérrez, and Enrique Sánchez. Comparison of era5 surface wind speed climatologies over europe with observations from the hadisd dataset. *International Journal of Climatology*, 41:4864–4878, 8 2021. doi:10.1002/joc.7103.

[38] Christopher W. Frank, Bernhard Pospichal, Sabrina Wahl, Jan D. Keller, Andreas Hense, and Susanne Crewell. The added value of high resolution regional reanalyses for wind power applications. *Renewable Energy*, 148:1094–1109, 4 2020. doi:10.1016/j.renene.2019.09.138.

[39] Luis Ramirez Camargo, Katharina Gruber, and Felix Nitsch. Assessing variables of regional reanalysis data sets relevant for modelling small-scale renewable energy systems. *Renewable Energy*, 133:1468–1478, 4 2019. doi:10.1016/j.renene.2018.09.015.

[40] Michael Borsche, Andrea K. Kaiser-Weiss, and Frank Kaspar. Wind speed variability between 10 and 116m height from the regional reanalysis cosmo-rea6 compared to wind mast measurements over northern germany and the netherlands. *Advances in Science and Research*, 13:151–161, 11 2016. doi:10.5194/asr-13-151-2016.

[41] Ruben Urraca, Thomas Huld, Ana Gracia-Amillo, Francisco Javier Martinez de Pison, Frank Kaspar, and Andres Sanz-Garcia. Evaluation of global horizontal irradiance estimates from era5 and cosmo-rea6 reanalyses using ground and satellite-based data. *Solar Energy*, 164:339–354, 4 2018. doi:10.1016/j.solener.2018.02.059.

[42] P J Meyer and J Gottschall. How do newa and era5 compare for assessing offshore wind resources and wind farm siting conditions? *Journal of Physics: Conference Series*, 2151:012009, 1 2022. doi:10.1088/1742-6596/2151/1/012009.

[43] V. Kumar, Aswathy Asok, Jesbin George, and M. Amrutha. Regional study of changes in wind power in the indian shelf seas over the last 40 years. *Energies*, 13:2295, 5 2020. doi:10.3390/en13092295.

[44] Kena Likassa Nefabas, Lennart Söder, Mengesha Mamo, and Jon Olauson. Modeling of ethiopian wind power production using era5 reanalysis data. *Energies*, 14:2573, 4 2021. doi:10.3390/en14092573.

[45] Samuel Andrés Gil Ruiz, Julio Eduardo Cañón Barriga, and J. Alejandro Martínez. Wind power assessment in the caribbean region of colombia, using ten-minute wind observations and era5 data. *Renewable Energy*, 172:158–176, 7 2021. doi:10.1016/j.renene.2021.03.033.

[46] Christoffer Hallgren, Jeanie A. Aird, Stefan Ivanell, Heiner Körnich, Ville Vakkari, Rebecca J. Barthelmie, Sara C. Pryor, and Erik Sahlée. Machine learning methods to improve spatial predictions of coastal wind speed profiles and low-level jets using single-level era5 data. *Wind Energy Science*, 9:821–840, 4 2024. doi:10.5194/wes-9-821-2024.

[47] Ellyess F. Benmoufok, Simon C. Warder, Elizabeth Zhu, B. Bhaskaran, Iain Staffell, and Matthew D. Piggott. Improving wind power modelling through granular spatial and temporal bias correction of reanalysis data. *Energy*, 313:133759, 12 2024. doi:10.1016/j.energy.2024.133759.

[48] Muhammad Abid Khan, Koji Dairaku, and Saurabh Kelkar. Assessing wind power generation potential over south asia using wind speed observation and reanalysis datasets. *Stochastic Environmental Research and Risk Assessment*, 39:1179–1207, 3 2025. doi:10.1007/s00477-025-02918-0.

[49] Giovanni Gualtieri. Reliability of era5 reanalysis data for wind resource assessment: A comparison against tall towers. *Energies*, 14:4169, 7 2021. doi:10.3390/en14144169.

[50] Bénédicte Jourdier. Evaluation of era5, merra-2, cosmo-rea6, newa and arome to simulate wind power production over france. *Advances in Science and Research*, 17:63–77, 6 2020. doi:10.5194/asr-17-63-2020.

[51] Michael R. Davidson and Dev Millstein. Limitations of reanalysis data for wind power applications. *Wind Energy*, 25:1646–1653, 9 2022. doi:10.1002/we.2759.

[52] G. S. Bhat, R. Morrison, C. M. Taylor, B. K. Bhattacharya, S. Paleri, D. Desai, J. G. Evans, S. Pattnaik, M. Sekhar, R. Nigam, A. Sattar, S. S. Angadi, D. Kacha, A. Patidar, S. N. Tripathi, K. V. M. Krishnan, and A. Sisodiya. Spatial and temporal variability in energy and water vapour fluxes observed at seven sites on the indian subcontinent during 2017. *Quarterly Journal of the Royal Meteorological Society*, 146:2853–2866, 7 2020. doi:10.1002/qj.3688.

[53] Mehul R. Pandya. Insat-3dr imager l3b land surface temperature product. doi:10.19038/SAC/10/3RIMG_L2B_LST.

[54] H. Hersbach. Global reanalysis: Goodbye era-interim, hello era5, 2019. URL: https://cir.nii.ac.jp/crid/1370302864780227330.

[55] Hans Hersbach, Bill Bell, Paul Berrisford, Shoji Hirahara, András Horányi, Joaquín Muñoz-Sabater, Julien Nicolas, Carole Peubey, Raluca Radu, Dinand Schepers, Adrian Simmons, Cornel Soci, Saleh Abdalla, Xavier Abellan, Gianpaolo Balsamo, Peter Bechtold, Gionata Biavati, Jean Bidlot, Massimo Bonavita, Giovanna De Chiara, Per Dahlgren, Dick Dee, Michail Diamantakis, Rossana Dragani, Johannes Flemming, Richard Forbes, Manuel Fuentes, Alan Geer, Leo Haimberger, Sean Healy, Robin J. Hogan, Elías Hólm, Marta Janisková, Sarah Keeley, Patrick Laloyaux, Philippe Lopez, Cristina Lupu, Gabor Radnoti, Patricia de Rosnay, Iryna Rozum, Freja Vamborg, Sebastien Villaume, and Jean-Noël Thépaut. The era5 global reanalysis. *Quarterly Journal of the Royal Meteorological Society*, 146:1999–2049, 7 2020. doi:10.1002/qj.3803.

[56] Hans Hersbach, Bill Bell, Paul Berrisford, Gionata Biavati, Andás Horányi, J Muñoz Sabater, Julien Nicolas, Carole Peubey, Raluca Radu, Iryna Rozum, et al. Era5 hourly data on single levels from 1979 to present. 2018. *Dataset. Retrieved September 1st*, 2019.

[57] H Hersbach, B Bell, P Berrisford, G Biavati, A Horányi, J Muñoz Sabater, J Nicolas, C Peubey, R Radu, I Rozum, et al. Copernicus climate change service (c3s) climate data store (cds). *ERA5 hourly data on single levels from 1979 to present*, 2018.

[58] Mathieu Pichault, Claire Vincent, Grant Skidmore, and Jason Monty. Characterisation of intra-hourly wind power ramps at the wind farm scale and associated processes. *Wind Energy Science*, 6:131–147, 1 2021. doi:10.5194/wes-6-131-2021.

[59] Karla Pereyra-Castro and Ernesto Caetano. Wind-ramp predictability. *Atmosphere*, 13:453, 3 2022. doi:10.3390/atmos13030453.

[60] P. C. SHARMA, R. C. VASHISTH, and VIJAY SINGH. Low temperatures and cold spells over rajasthan during two decades. *MAUSAM*, 56:711–718, 7 2005. doi:10.54302/mausam.v56i3.1005.

[61] Abdüsselam Altunkaynak, Tarkan Erdik, İsmail Dabanlı, and Zekai Şen. Theoretical derivation of wind power probability distribution function and applications. *Applied Energy*, 92:809–814, 4 2012. doi:10.1016/j.apenergy.2011.08.038.

Supplementary Figures

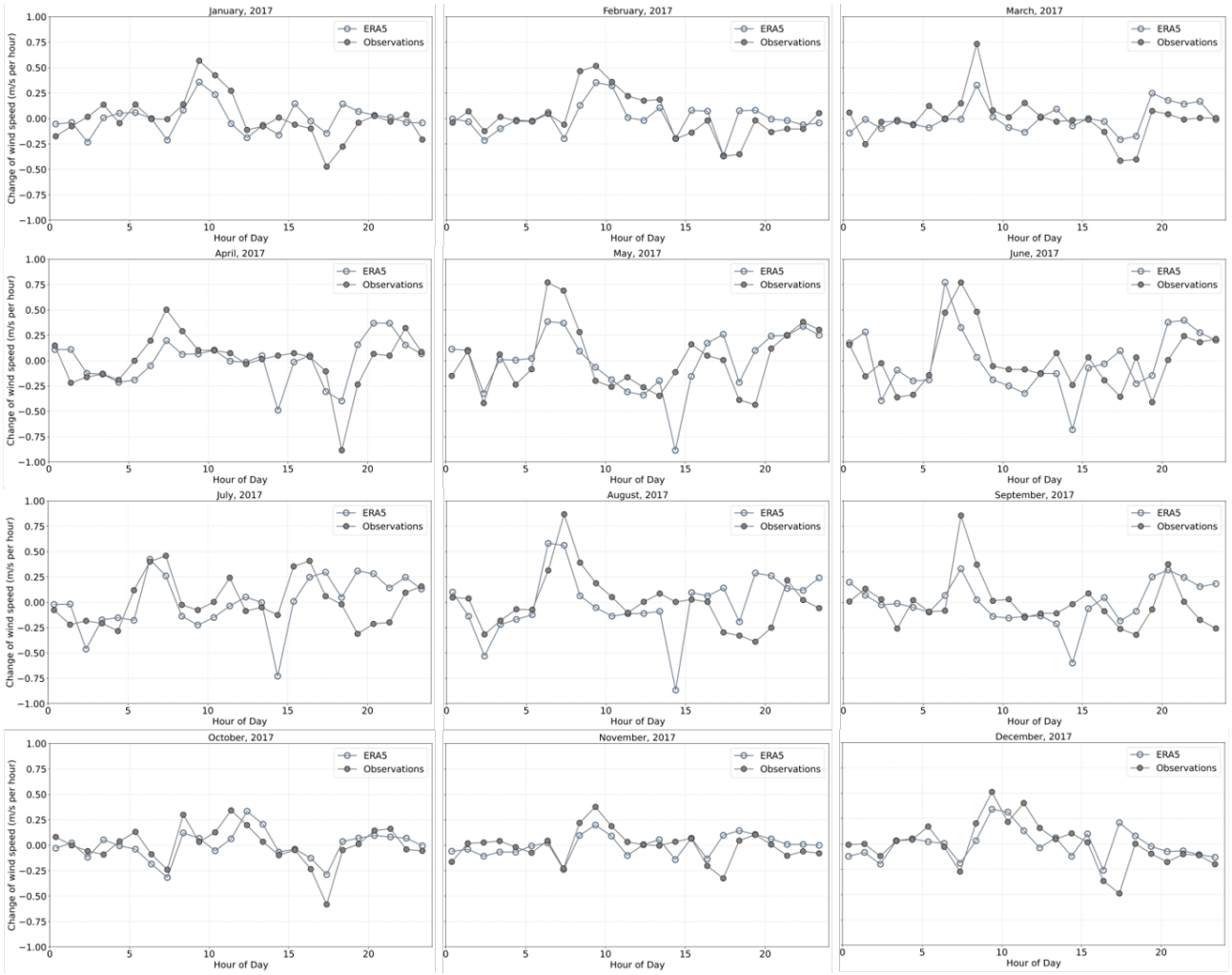

Figure 11: **Supplementary Figure S1.** Observed change of wind speed per hour for different months in 2017 compared with ERA5 reanalysis data.

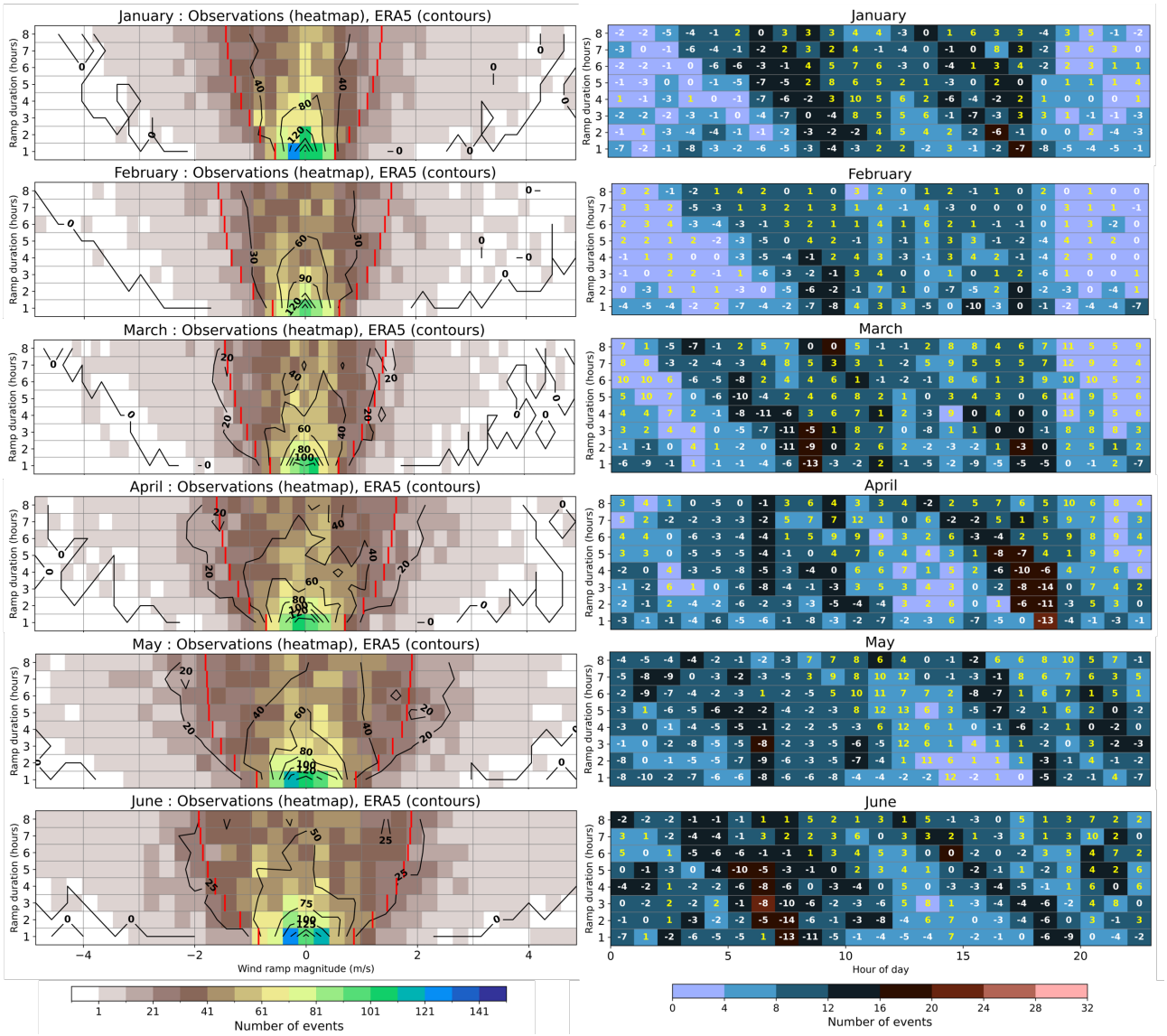

Figure 12: **Supplementary Figure S2a.** Change of wind speed over different durations and their diurnal occurrence for months January to May.

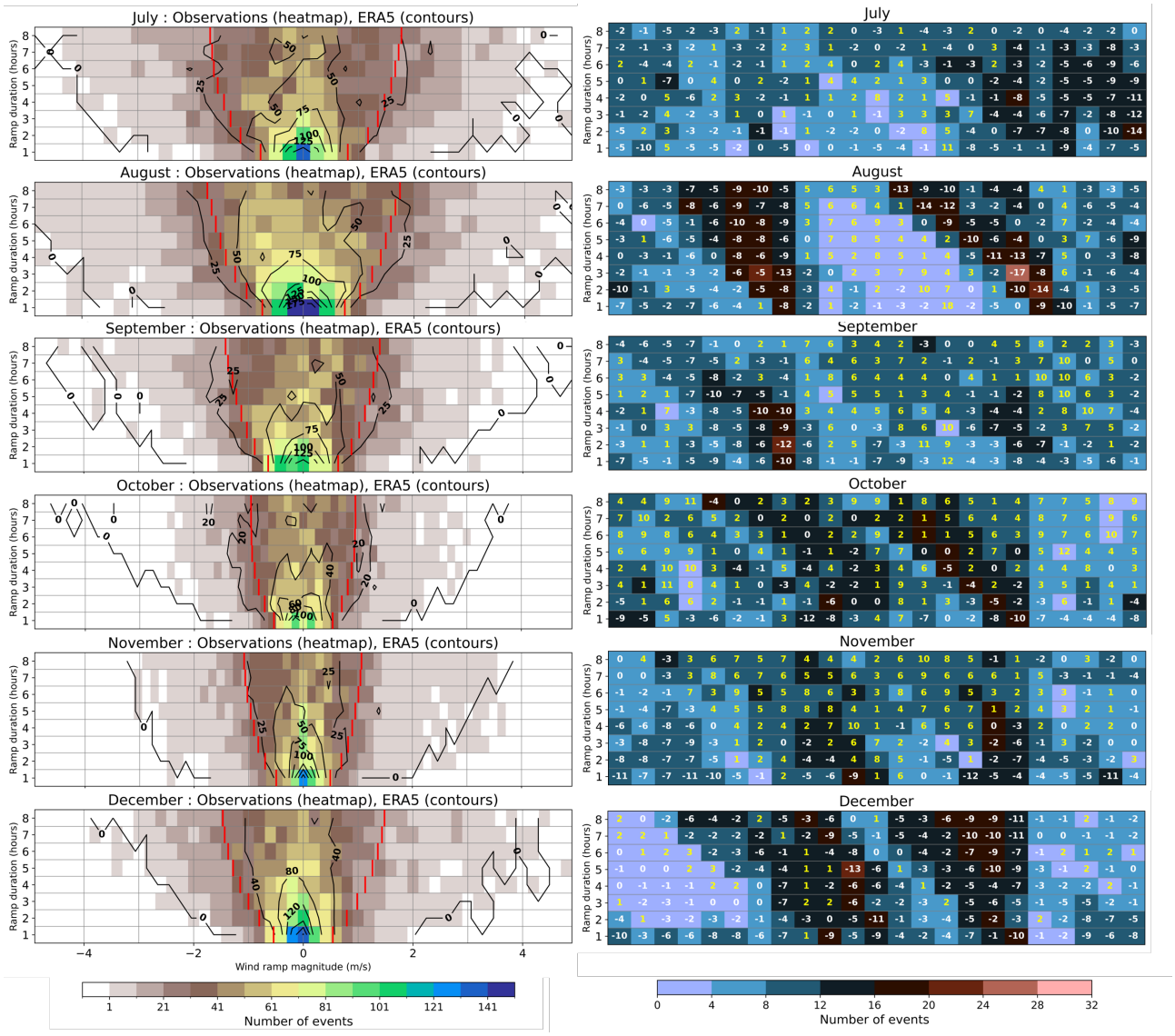

Figure 13: **Supplementary Figure S2b.** (cont. from previous figure) Change of wind speed over different durations and their diurnal occurrence for months June to December.

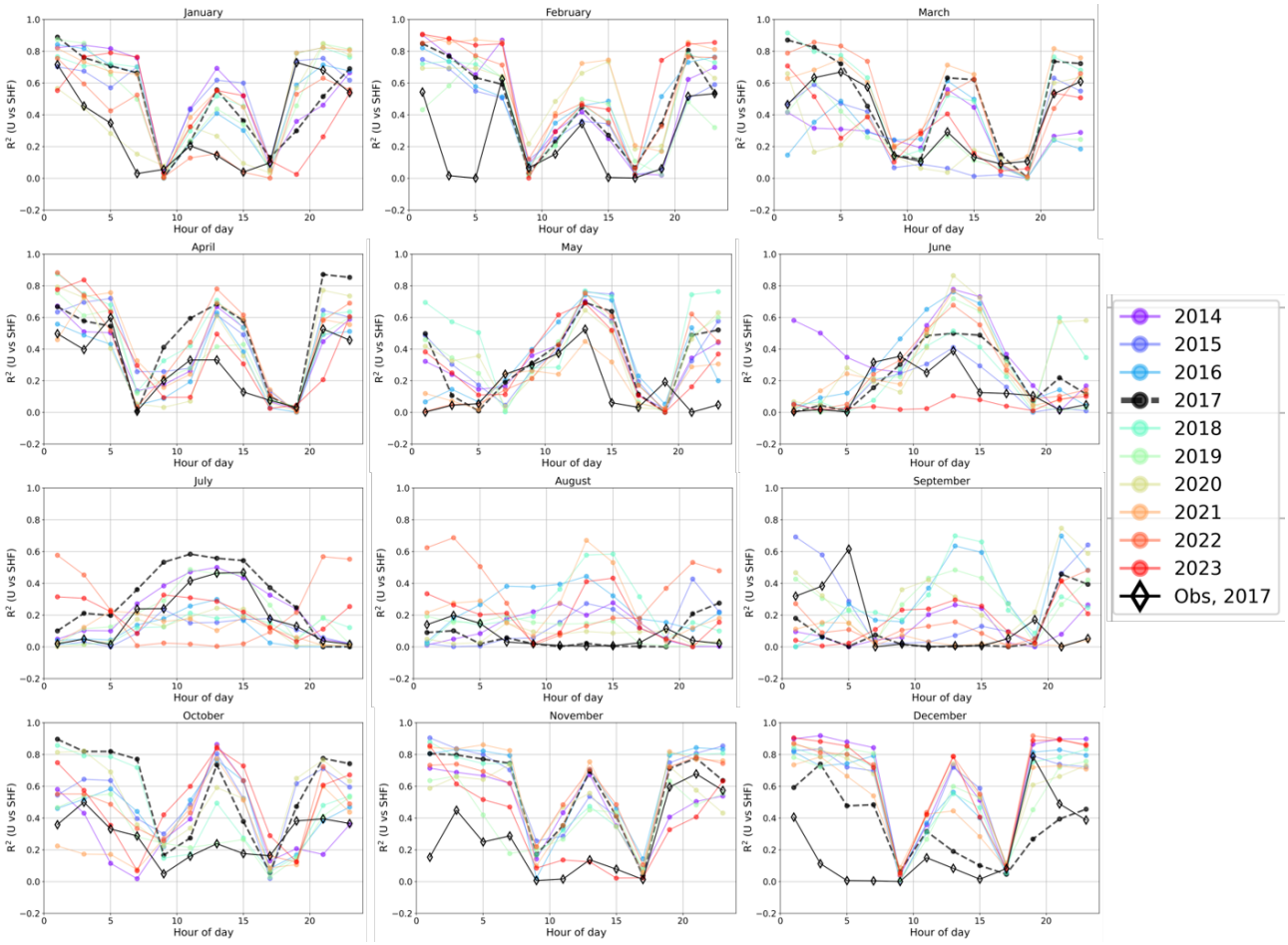

Figure 14: **Supplementary Figure S3.** Diurnal variation of the coefficient of determination for the linear relationship between surface sensible heat flux and wind speed as seen in ERA5 reanalysis for ten years from 2014-2023, compared with the pattern in observations during 2017.

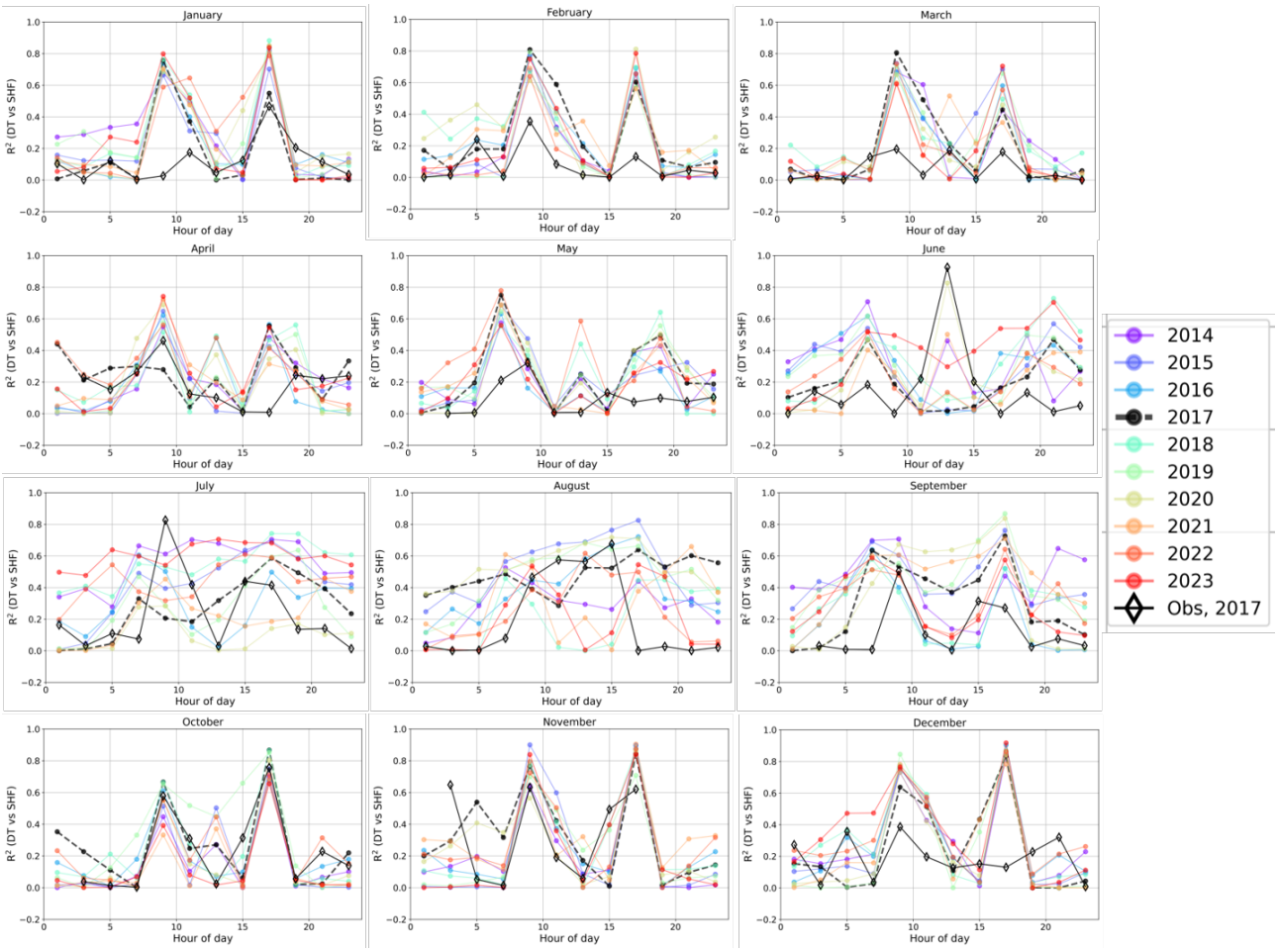

Figure 15: **Supplementary Figure S4.** Testing the applicability of Townsend's regime, proposed also as the weakly-forced convective regime previously. Diurnal variation of the coefficient of determination for the linear relationship between surface sensible heat flux and temperature different as seen in ERA5 reanalysis for ten years from 2014-2023, compared with the pattern in observations during 2017.